STRESS ANALYSIS OF A POINT ABSORBER WAVE ENERGY CONVERTER

by

Tanuj Gupta

A thesis submitted to the faculty of
The University of North Carolina at Charlotte
in partial fulfillment of the requirements
for the degree of Master of Science in
Mechanical Engineering

Charlotte

2019

Approved by:

_____

Dr. Alireza Tabarraei

_____

Dr. Navid Goudarzi

_____

Dr. Russell Keanini

ABSTRACT

TANUJ GUPTA. Stress analysis of a point absorber wave energy converter. (Under the direction of DR. ALIREZA TABARRAEI)

Ocean wave energy is vastly untapped renewable source even-though it has the highest energy density. In this work, a full scale point absorber ocean wave energy converter model (WEC) with hydraulic power take-off (PTO) is developed. The hydrodynamic forces collected from the National Data Buoy Center near North Carolina shore is used to study the stresses endured by the WEC model. The stresses are evaluated using a commercial finite element method (FEM) software ABAQUS. A linear elastic model is implemented to account for the material behaviour in addition to the Hilbert-Hughes-Taylor-α (HHT-α) method to understand the dynamic response of the WEC. The displacement along with the effect of PTO damping are validated by other numerical as well as experimental results.

The stresses and deformation on the WEC are also studied. Furthermore, a study involving PTO damping and angle of WEC arm and their effect on the fatigue life is also carried out. The results indicated that WEC arm has maximum deformation whereas bracket has the least. However, the stress on WEC parts is dependent on the PTO damping as well as the arm angle. The fatigue life of the PTO system can be significantly increased by increasing the PTO damping. Moreover, fatigue life can also be increased by increasing the arm angle. These analyses are not only cost effective but also provide intuitive understanding to optimize the design process of WECs

DEDICATION

I am grateful to always have full support of my family members Lalan Rauniyar, Priti Rauniyar, Payal, Pragati and Akshita. I dedicate my masters to my family.

ACKNOWLEDGEMENTS

I would like to thank my advisor Dr. Alireza Tabarraei for his guidance and mentoring throughout my master's degree program. His support, critical reviews and encouragement helped me achieve a research degree. I am thankful to Dr. Navid Goudarzi for making me a part of his work. I would like to extend my gratitude to Dr. Russel Keanini for being a part of my thesis committee.

I am grateful to Dr. Shank Kulkarni, Mohan Raja, Imrul Reza Shishir, Dhanooj Booba, Sam Sutherson and all other lab members for their encouragement and reviews.

TABLE OF CONTENTS

LIST OF TABLES

LIST OF FIGURES

LIST OF ABBREVIATIONS

BEM Boundary element method

CSA Cross-sectional area

FE Finite element

FEA Finite element Analysis

FEM Finite element method

PDE Partial Differential Equation

PTO Power-take off

RM3 Reference Model 3

WEC Wave Energy Converter

CHAPTER 1: INTRODUCTION

Ocean waves are primarily formed by the wind that is a result of thermal air currents. These are generated when warm air above water level rises and is replaced by cooler dense air. The contribution of wind to create the waves is also attributed to the rotation of the earth and tidal current to the moon's gravitational pull. The ocean waves thus formed can be broadly categorized into linear and non-linear waves. Linear waves have a wave height to wavelength ratio of 1/50 or less [5]. It can be approximated using a sinusoidal profile as shown in Figure 1.1. In the case of non-linear waves, the wave profile is affected by the sea floor. It has a narrow crest and a broader trough [6].

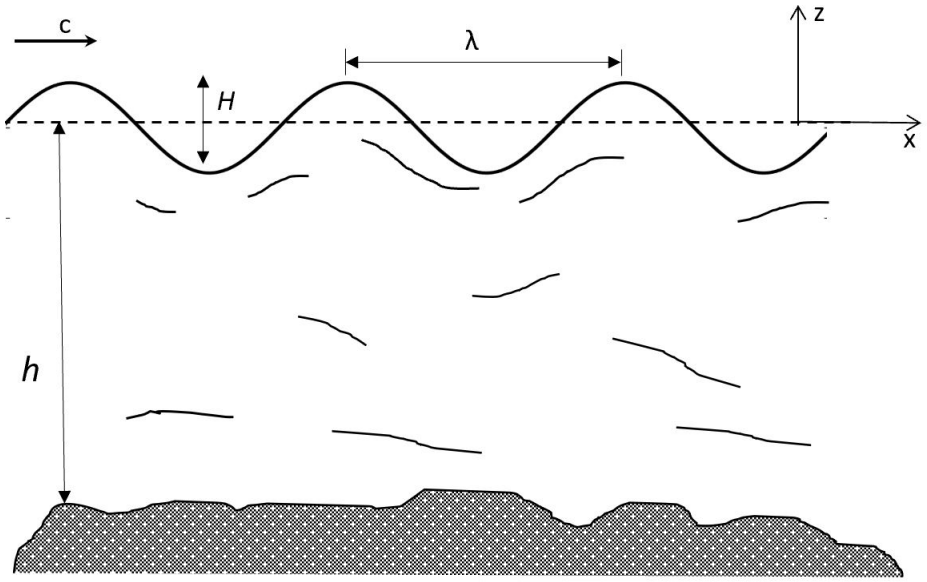

Figure 1.1: A linear wave- one having sinusoidal profile

As the need for renewable energy grows alternative reliable sources of energy needs to be accessed. This is where ocean wave and particularly energy from these waves come into the picture. Ocean wave being more constant, predictable and having

higher energy density makes it a promising renewable energy source [7]. Melikoglu and Mork [8,9] present a review of the ocean wave energy resources and potential on a global scale. The estimated global wave-power output is about 10 TW. Although the concept of obtaining energy from ocean waves is not a new one, it has not yet been fully developed as an energy source. One of the earliest recorded patents of wave energy conversion devices is by Girard and Sons in France that dates back to 1799 [10]. In Britain, more than 300 patents of wave-powered devices have been documented by Leishman between 1855 and 1973 [11]. In the 1940s, Yoshio Masuda developed a form of wave energy converter, known today as oscillating water column, that was commercialized in Japan and later in the US [12]. In the 1970s, the surging oil prices pushed the research of renewable energy sources and in an effort to find alternate source S. Salter designed a cam-shaped device that would rotate in to and fro motion due to the incoming wave to generate electricity [13]. It showed a promising efficiency of about 40% when driving electronic dynamometer. In 1981, McCormick published a book on Ocean Wave Energy Conversion where he described the nature of linear and non-linear waves and various techniques to extract and store ocean wave energy [5]. These researchers were among the first to realize the commercial capability of ocean wave and bring it to the attention of the international community.

The Electric Power Research Institute estimates that 898-1229 TWh/yr energy can be extracted via ocean waves near the coastal areas of US alone [2]. Additionally, nearly 50% of the US population resides close to the coastal region which makes it a more suitable form of renewable energy [14]. Various collaborative programs on wave energy conversion in the US along with accessibility within different geographic regions is discussed by Bedard et al. and Previsic et al. [14,15]. However, European countries lead in terms of the number of operational WEC deployed. Clement provides the research and development of WECs done by European nations during the 1990s [16]. In contrast to other renewable sources such as hydropower, wind and solar,

ocean wave energy are the least developed in commercial sector [17]. In the past few decades, more than 100 conceptual design and models have been developed with varying energy conversion principles [18]. However, only a handful of the prototype has been deployed, current major WEC projects around the globe are presented by Titah-Benbouzid [1]. A thorough review of these WEC technologies is presented by Falcao [19].

The major advantage of wave energy over other renewable sources is that it has the highest energy density [16]. Moreover, different principles can be applied to extract the energy that leads to several WEC designs. Falnes provides a review of these energy extraction methods [20]. Although based on working principle WECs is divided into six categories only four are widely used, these include attenuators, oscillating wave surge converters, oscillating water column and point absorber [21]. Among these oscillating water columns and point, absorbers are at a more advanced stage. Attenuators are semi-submerged structures that maximize power absorption through heaving motion of multiple cylindrical shaped objects connected via hinge joint [22]. Oscillating wave surge converters are near-shore WEC that generate power through the surge of waves that travels horizontally near the shore [23]. It has pitching flaps that oscillate orthogonally to the wave direction through a hinge [24]. In the case of the oscillating water column, the air trapped inside a chamber is pushed back and forth due to the incident waves. This motion of air is passed through a bidirectional turbine that generates electricity. Point absorbers have a float, commonly known as a buoy, that oscillates vertically due to the heaving wave motion. The float is connected to a PTO system typically a hydraulic system for power conversion.

One of the challenges in designing the WECs as mentioned above is the complexity involved in modeling the hydrodynamic forces. It requires modeling convoluted diffraction and radiation wave phenomenon because of which earlier designs were mainly focused on determining the hydrodynamic loads [19]. The hydrodynamic

forces on a body interacting with fluid is resolved into diffraction and radiation forces. Diffraction force is caused due to the incident wave whereas radiation forces are due to the motion of the body. Additionally, the body also experiences a hydro-static force due to the undisturbed free surface fluid. Furthermore, to determine the structural loads due to these forces on WEC, fluid-structure interaction (FSI) needs to be studied. This requires coupling of numerical models for fluid problems with numerical models for structural problems. FSI arises in several fields including marine structure, structural acoustics, ship hydrodynamics. In a paper by Tallace [25], a numerical framework for coupling fluid-structure interaction involving structure with large displacement was introduced. The algorithm developed uses Arbitrary Lagrangian Eulerian (ALE) formulation for the fluid part and total Lagrangian method for the elastic structure region. This was implemented for a hydro-elastic shock absorber problem with reasonable accuracy.

On the structural part, the difficulty lies in designing the power-take-off (PTO) system. PTO is a characteristic of a WEC that determines the working principle used in the conversion of ocean energy to useful energy. PTO of deployed WECs is shown in Table 1.1. In a recent experimental work by Zang et al. [26] the effect of linear PTO damping on the power performance for a heaving buoy was studied. It was observed that the buoy had maximum displacement and velocity for structural damping only. However, the phase difference between buoy velocity and incoming wave decreases with increase in PTO damping. Additionally, theoretical studies indicate that for maximum power absorption the point absorber WEC oscillating in heave should be in a near resonance condition, i.e. its frequency should match the incoming wave frequency. The resonance condition was achieved when the damping ratio of PTO to the WEC structure was nearly twice. A series of experiments with varying period and wave height was also conducted. Wen et al. [27] proposed a geometry optimization method based on linear potential flow theory and the response

surface method to maximize the energy absorption for a single body point-absorber. Boundary element method (BEM) was implemented for hydrodynamic analysis. Additionally, the absorption power spectrum with different PTO damping was studied, and the optimal damping coefficient was determined. Kim et al. [28] studied numerical and experimental aspect of a hemispheric point-absorber WEC design similar to that in this study. A hydraulic PTO consisting of a hydraulic cylinder (HC) and the hydraulic motor was installed. Power generation and energy loss were studied. However, in all the cases structural loads on the WEC was not determined.

Table 1.1: Power Take Off systems [1].

WEC	PTO	Generator
POWERBUOY	Point Absorber	Permanent magnet synchronous generator
OCEANLINX	Oscillating water column	Cage Induction motor
PICO	Oscillating water column	Doubly-fed induction motor
LIMPET	Oscillating water column	Cage Induction motor
PELAMIS	Attenuators	Cage Induction generator
AWS	Direct drive	Linear permanent magnet
OYSTER	Oscillating wave surge	Cage Induction motor
WAVE DRAGON	Over-topping	Permanent magnet synchronous generator

In addition to the complexity involved in the PTO system, the structural design of the WEC needs to sustain extreme loads in the ocean. Jennifer et al. considered two simpler WEC models for early design analysis [18]. First one to be a free-floating slender barge and the second one to be fixed- bottom column. These were approximations for Wave-Carpet and single-body point-absorber type WEC design respectively. Generalized body-modes approach, a linearized frequency domain method, was com-

pared with high-fidelity FSI approach for stress and deflection on the flexible body. Although the results from a generalized body approach were within 10 % of the FSI approach there lies a significant difference between the computational time. The simulation time of FSI approach was orders of magnitude higher than the body-modes approach. Nonetheless, the stress analysis was performed for a somewhat simpler design and may result in higher inaccuracy when complex geometry WEC in conjunction with PTO systems is considered.

The structural loads for a WEC model were determined using an experimental setup by Sandia National Laboratory [2]. The loads on a scaled Reference Model 3 (RM3) WEC design was analyzed in a wave tank of 68 m long and 2.4 m wide. These forces were scaled up and input into finite element analysis models to determine the structural load. However, fatigue testing on the model was not performed. A similar setup was presented by Zurkinden et al. where a laboratory model representing the Wavestar prototype WEC was subjected to structural loads in a wave tank [29]. Here, the fluid-structure interaction between a hemispherically shaped float was taken into consideration. Estefen et al. [30] conducted small scale experimental as well as full-scale numerical design analysis for a recently deployed onshore WEC. The structural loads considering dynamic, extreme and fatigue loading were evaluated.

Methodologies for evaluating structural loads on deformable WEC have yet to be fully considered and incorporated in the WEC design process [18]. This study focuses on developing a numerical model for an RM3 type WEC design to determine the structural loads. In contrast to experimental setup that can be expensive, numerical models can be replicated by considering various material, float positions and other variables such as damping and stiffness of the power take-off system. It makes the process of optimization more feasible thus leading to a better structural design. It also ushers to the possibility of commercialization.

Chapter 2 presents a summary of the hydrodynamic forces experienced by the WEC

along with the description of the WEC model. Chapter 3 dives into the methodology involved in evaluating the structural dynamics of the WEC starting with a discussion on finite element analysis followed by its mathematical formulation. Additionally, material constitutive model, assembly of the WEC parts along with dynamic analysis and loading are discussed. In chapter 4, validation cases involving the displacement and velocity of the arm and PTO damping is compared. In addition to that, stresses and deformation on all the parts are discussed along with the parametric study of the effect of damping and floater. Furthermore, fatigue life is also determined. Finally, after obtaining all the results conclusion is summarized.

CHAPTER 2: WEC-Forces And Model

2.1 Hydrodynamic Forces

To build an optimum design, wave characteristics needs to be studied and subsequently the forces that arise. Wave characteristic is defined by wave height and wave period. The wave properties varies depending on the location of the site under consideration. In this study wave characteristics of North Carolina shore collected from two buoys (US430 and US192) from National Data Buoy Center is taken into account. Department of Energy (DOE) along with Sandia National Laboratory(SNL) and National Renewable Energy Laboratory (NREL) developed the Reference Model Project (RMP) as shown in table 2.1. It categorizes the types of wave energy converter based on the wave characteristics as well as the techniques involved in the energy extraction. These models besides the open source WEC-Sim code developed by DOE is used to improve the WEC design. Following the limitation of post-processing involved in the WEC-sim, for the RM3 defined by DOE, the hydrodynamics forces on the model is calculated using StarCCM+, a commercial CFD software, by Akshith [4]. As mentioned earlier the hydrodynamic force is a combination of diffraction forces, radiation forces and force due to undisturbed wave. Using a 3-D boundary element

Table 2.1: DOE defined Reference Models [2].

Reference Model	Type
1	Tidal current turbine
2	River current turbine
3	Wave point absorber
4	Ocean current turbine
5	Oscillating surge - WEC
6	Floating Oscillating surge - WEC

method, based on Volume of Fluid method, Akshith calculated the diffraction forces on a scaled spherical float of diameter 250 mm. To get a better understanding on the CFD software used, boundary element method and volume of fluid method reader is advised to refer to [31–33].

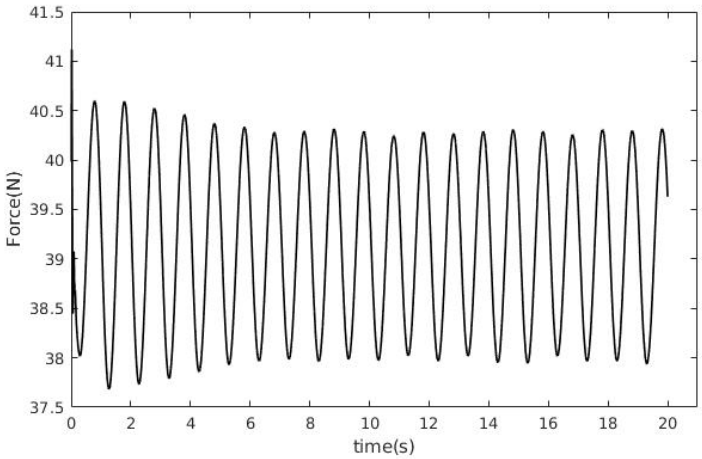

Figure 2.1: Heave force [4].

The forces measured on the scaled float was scaled up using Froude number scaling since the gravitational effects are significant as compared to surface tension and viscosity.

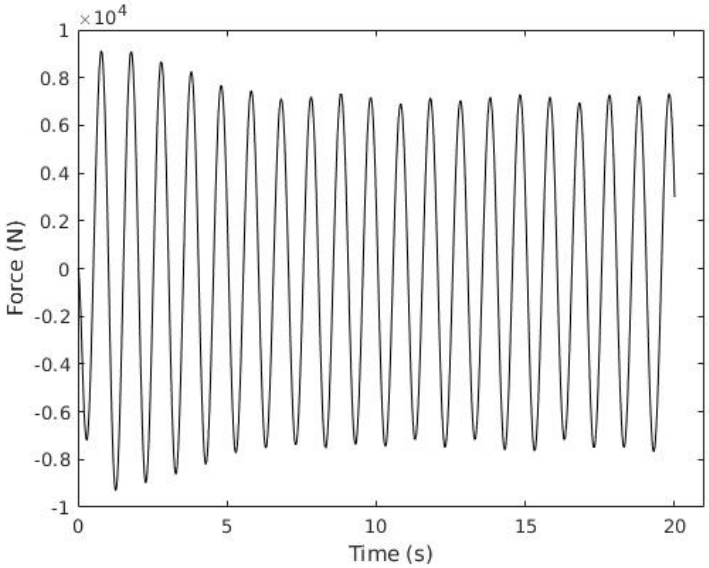

Figure 2.2: Scaled heave force

2.2 WEC Model

In this study, the WEC model considered was designed by the National Ocean Technology Center(NOTC). The WEC consists of a floater arm, piston, hydraulic cylinder, and bracket as shown in figure 2.3. One end of the arm is connected to the floater(not shown here), and the other end is hinged to a platform. The floater's arm converts the heaving motion of the floater. The piston connected to the arm then transfers this into axial motion with respect to the HC. The HC is hinged to a bracket that is rigidly fixed to the platform. The axial motion of the piston pushed the hydraulic fluid inside the HC which in turn is connected to a hydraulic pump for energy conversion. The following points are defined as the scope in this study:

- Only heaving forces due to the waves are considered.
- .The heaving forces acts through the point where the floater's arm is connected to the buoy.
- Power conversion process and energy loses are not investigated.
- The primary focus is on stresses acting on the WEC parts due to the heaving force.
- Effect of power take of damping and floater's arm angle on stresses in studied.
- Variation in fatigue life due to PTO damping and floater's arm angle is studied.

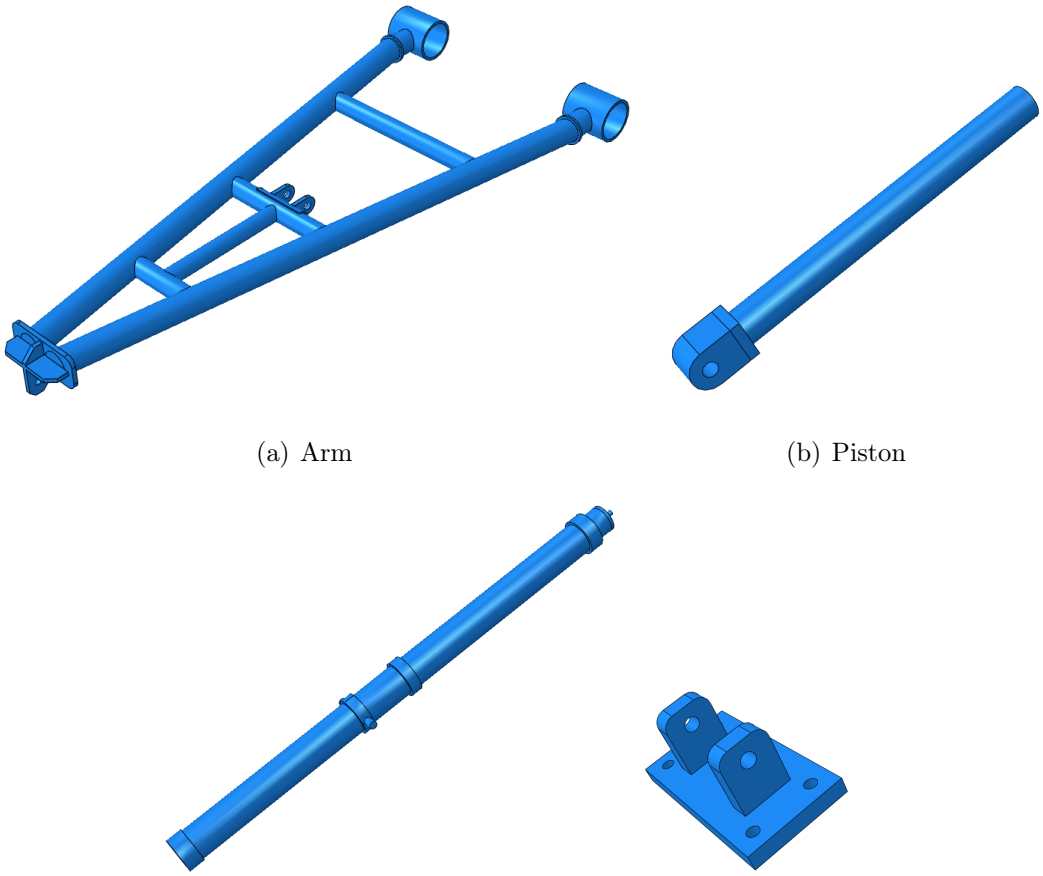

(a) Arm (b) Piston

(c) Hydraulic Cylinder (d) Bracket

Figure 2.3: WEC parts

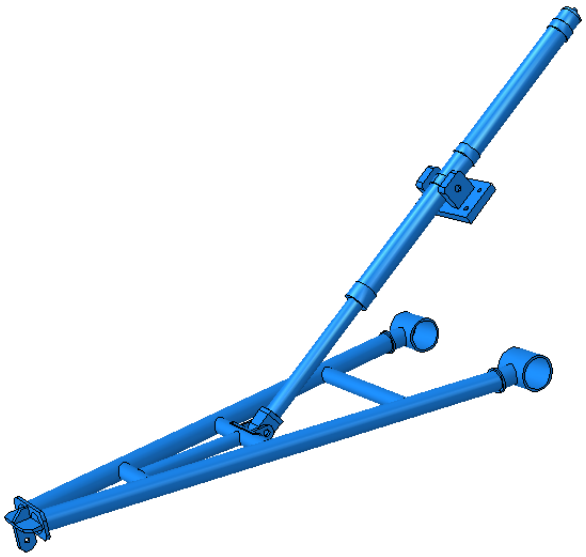

Figure 2.4: Point absorber WEC

CHAPTER 3: FINITE ELEMENT ANALYSIS

3.1 FEM in structural dynamics

Analytically determining the solutions to partial differential equations (PDEs) often may not be possible. Finite element method (FEM) is a widely used numerical technique to approximate the solution to PDEs. In this method, the spatial domain is discretized using shape functions (basis functions) followed by time discretization for dynamic problems. One of the significant advantages of this method is that it applies to any given shape of a structure with varying material properties. It is widely used in structural dynamics problems. However, the discrepancy in analytical and actual results may arise due to simplified geometry or inaccurate boundary conditions [34]. Kim et al. [35] proposed an improved second order accurate implicit numerical method for one-dimensional structural dynamics analysis. The governing dynamic equation was developed with respect to displacement and given PDE terms, which directly satisfied the natural boundary conditions. Nonetheless, because of the versatility and accuracy of FEM, it is utilized in this study.

In addition to that, all the parts in this study are considered to deformable (flexible), i.e. they undergo finite strain. Flexible multibody are connected by joints that are constrained and experience large displacement (or rotation) along with elastic deformation. Incorporating flexible multibody in FEM was pioneered by Besseling [36], and later was developed by [37–39]. Shabana [40] provides a review and development of flexible multibody dynamics including formulation, simulation, and application in computer graphics. This study incorporates the idea of flexible multibody and FEM.

3.2 Finite Element Formulation

The finite element (FE) formulation involves deriving weak form of the strong form of the momentum balance governing equation, a PDE. The strong form is given as,

$$\frac{\partial \sigma_{ij}}{\partial x_j} + \rho b_i = \rho \dot{v}_i \tag{3.1}$$

The boundary conditions are,

$$\sigma_{ij} n_j = t_i \quad on \quad \partial\Omega_t \quad and \quad u_i = \bar{u}_i \quad on \quad \partial\Omega_u \tag{3.2}$$

Here, σ_{ij} is the stress tensor, ρ is the density, b_i is the body force per unit volume, $\dot{v}_i$ is the acceleration, n_j is the unit outward normal of the boundary surface, t_i and $\bar{v}_i$ are the prescribed traction and displacement on the surface $\delta\Omega_t$ and $\delta\Omega_u$ respectively. From the principle of virtual power [41] the weak form (variational form) of the above strong form can be written as,

$$\int_\Omega \frac{\partial(\delta v_i)}{\partial x_j} \sigma_{ij} d\Omega + \int_\Omega \delta v_i \rho \dot{v}_i d\Omega = \int_\Omega \delta v_i \rho b_i d\Omega + \int_{\partial\Omega_t} \delta v_i \rho t_i dS \tag{3.3}$$

Here, δv_i is the virtual velocity(test function). The LHS of equation 3.3 represents the internal power that constitutes of the virtual stress power and virtual kinetic power whereas the RHS represents the virtual external power due body force and traction on the surface. Thus, equation 3.3 can be simplified as,

$$\delta P^{int} + \delta P^{kin} = \delta P^{ext} \tag{3.4}$$

In this study, updated Lagrangain formulation is utilized, a popular method in solid mechanics [42]. Here, the integrals and derivatives in the aforementioned weak form are taken in the spatial coordinates (current configuration). Discretizing the current domian Ω into FEs Ω_e the approximate position, velocity and acceleration for each element can be expressed as,

$$x_i(X,t) = N_I(X) x_{iI}(t) \tag{3.5}$$

$$v_i(X,t) = N_I(X) v_{iI}(t) \tag{3.6}$$

$$a_i(X,t) = \dot{v}_{iI}(t)N_I(X) \tag{3.7}$$

Here, $N(X)$ is the shape function in material coordinate system that can be mapped to spatial coordinates as $X = \phi^{-1}(x,t)$. The virtual internal power in the equation 3.4 can be expressed as a scalar product of internal nodal forces and virtual velocities. Using the approximation in equation 3.6 the virtual internal power for an element can be written as,

$$\delta P^{int} = \delta v^T f^{int} = \delta v^T \int_\Omega \frac{\partial N_{iI}}{\partial x_j}\sigma_{ij}d\Omega = \delta v^T \int_\Omega B_{Ij}\sigma_{ij}d\Omega \tag{3.8}$$

Here, B_{Ij} is the matrix of shape function derivatives. Similarly, the virtual external power and kinetic energy is determined as,

$$\delta P^{ext} = \delta v^T \int_\Omega N_{iI}\rho b_i d\Omega + \delta v^T \int_{\partial\Omega_t} N_I \bar{t}_i d\Omega_t \tag{3.9}$$

$$\delta P^{kin} = \dot{v}_{iJ} \int_\Omega N_I N_J \rho d\Omega \tag{3.10}$$

In equation 3.10 the quantity inside the integral represents the mass matrix and is written as,

$$M_{ijIJ} = \delta_{ij} \int_\Omega \rho N_I N_J d\Omega \tag{3.11}$$

Finally, the global equation of motion in terms of mass matrix, acceleration, external force vector and internal force vector can be written in the form given by equation 3.12.

$$Ma + f^{int} = f^{ext} \tag{3.12}$$

3.3 FE Modelling in Abaqus

Abaqus is a research based FEA tool used particularly in aerospace and automotive industries. The customization of material properties makes it a popular software for FE modelling in academia. In this study, it is not only used to build the model design but also carry out the FEA.

3.3.1 Material Constitutive Model

All the materials in the WEC model are considered as linear elastic material. The constitutive equations give a relation between the deformation of body, characterized as strain, with the stress due to the deformation. The constitutive equation for an elastic material in its general form can be written as,

$$\sigma_{ij} = C_{ijkm}\epsilon_{km} \tag{3.13}$$

Here, σ is the stress tensor, C is a fourth order tensor with 81 components and ϵ is the strain tensor. Furthermore, the material is considered to be homogeneous without any internal defects. Because of which the components of fourth order tensor is reduced to 36 with all being constants [43]. Moreover, for isotropic material the components of C does not change with orthogonal transformation. This reduces the number of components to 2. The stress tensor can then be expressed as,

$$\sigma_{ij} = \lambda\delta_{ij}\epsilon_{kk} + 2\mu\epsilon_{ij} \tag{3.14}$$

Here, δ_{ij} is the Kronecker delta, λ and μ are Lame's constants. Equation 3.14 defines the well established Hooke's law. However, in Abaqus the stress is calculated using Young's modulus and Possion's ratio that can be expressed in terms of Lame's constant as,

$$E = \frac{\mu(3\lambda + 2\mu)}{(\lambda + \mu)} \tag{3.15}$$

$$\nu = \frac{\lambda}{2(\lambda + \mu)} \tag{3.16}$$

Thus, equation 3.14 can be written in terms of these parameters as,

$$\sigma_{ij} = \frac{E}{1+\nu}(\epsilon_{ij} + \nu\delta_{ij}\epsilon_{kk}) \tag{3.17}$$

S355 steel, which is a common material for offshore and structural application [44], was chosen for this study. The material properties of S355 steel are given in table 3.1.As the forces on the model are below elastic limit of the material the linear elastic

model was adopted for stress analysis.

Table 3.1: Mechanical properties of S355 Steel.

Property	Value
Young's Modulus(GPa)	200
Density(kg/m^3)	7850
Possion's ratio	0.3
Yield strength (MPa)	355

In this study, von-Mises stress is used to define the yielding of the material. It is widely used criterion for linear elastic material. It is based on the maximum distortion energy associated with change in shape of material for a given strain. The body starts to yield when stress on the material is greater than the stress based on this criterion. For a simple uni-axial tension test material will start to yield when the stress is greater than the elastic limit of the material.

The yield function can be expressed mathematically as,

$$J_2 = k^2 \tag{3.18}$$

Here, k is yield stress of material in shear given by experiment and J_2 for a three-dimension stress state is given as,

$$J_2 = \frac{1}{6}((\sigma_1 - \sigma_2)^2 + (\sigma_2 - \sigma_3)^2 + (\sigma_1 - \sigma_3)^2) \tag{3.19}$$

Here, σ_i, $i = 1, 2, 3$ are the principal stresses. For pure shear stress state von-Mises yield criterion is given as,

$$k = \frac{\sigma_y}{\sqrt{3}} \tag{3.20}$$

Here, σ_y is the yield stress. Thus using equations 3.19 and 3.20 the von-Mises stress can be written as,

$$\sigma_v = \sqrt{3}k = \sqrt{3J} \tag{3.21}$$

Finally, the von-Mises criterion can be expressed as,

$$\sigma_v \geq \sigma_y \tag{3.22}$$

The yield stress of S355 steel is 355 MPa as shown in table 3.1. Therefore, the material will start to yield and have a irrecoverable strain if the stress in the material due to the load exceeds this stress.

3.3.2 Assembly

All the parts, floater arm, piston, HC and bracket are modeled in Abaqus CAE using various extrusion techniques. The modeled parts are then assembled in the Assembly module using constraints to put them in place. The joints are explicitly assigned to parts using connector assignment to define the relative motion between the parts. There are two kinds of joint used in model one is hinged, and the other is a translator. These are modeled using a wire feature and given a specific property as required. The floater's arm is hinged to the ground. The piston and floater arm is also connected using a hinge joint. The joint is assigned using a wire feature and is connected to piston and arm using an MPC(Multi-Point Constraints). The hinge joint is assigned to mimic the motion between HC and bracket. A translator joint is assigned between piston and HC to represent the axial movement between the two parts. This joint is given a damping coefficient to represent the damping of the piston due to the hydraulic fluid and a stiffness coefficient to represent the stiffness of the WEC.

3.3.2.1 Joints

The multi-body system consists of 4 parts, and appropriate joints are used to restrict the degrees of freedom and define the relative motion between the parts.

3.3.2.2 Translator joint

A translator spring with local coordinate system was defined to replicate the oscillatory motion between piston and hydraulic cylinder. Additionally, the connector

was given a linear damping as well as linear stiffness property. It was so done because the hydraulic fluid present inside the will have a damping effect on the piston. The stiffness property is the characteristic of the power take off system.

3.3.2.3 Hinge joint

The hinge joint facilitates the vertical oscillatory motion of the floater's arm. The arm is hinged to the ground, in practicality the arm is hinged to the ship. Furthermore, the piston is connected to the arm using a hinge joint.

3.3.2.4 Multi-point constraints

Connectors in the Abaqus are used in conjunction with MPC. Abaqus provides a range of MPC type depending on the type of analysis. For this study, MPC Beam Type is used. It provides a rigid beam between two nodes to constrain displacement and rotation at the first node to the displacement and rotation at the second node. It resembles the presence of a rigid beam between the two nodes. For the WEC model, MPC is used to constrain the rotation of the floater's arm to the axis of the hinge motion. Additionally, it is also used in the hinge connector between the piston and floater arm and translator connector between piston and cylinder.

3.3.3 Contact Algorithm

Surface to surface based discretization is used to define the contact between the inner region of HC and outer region piston in contact. Abaqus provides with an option to choose master and slave surfaces. For this study, the HC is chosen to be the master surface and piston to be the slave surface as the HC has more surface area. The choice has minimal effect when used in conjunction with the above discretization. It is computationally expensive at it enforces the contact constraints taking an average over the regions on a particular node. The cost is reduced by seeding both the regions with relatively same mesh size, with a difference of 0.008m. The advantage of using the surface to surface discretization is that it follows Newton's third law of

motion. The net force acting on each surface are of equal magnitude but opposite in direction. The interaction between piston and HC is defined using surface-to-surface based interaction in Abaqus with Finite Sliding formulation. This formulation allows relative motion between the deformable inner surface of HC and the outer surface of the piston. The piston and HC are fitted using a clearance fit of 0.001mm. In this study, for the tangential behavior, Coulomb fiction model is considered. It relates the maximum shear stress to the contact pressure through the coefficient of friction. The two surfaces in contact can carry shear stresses up to the maximum allowable shear stress across their surface before they start sliding relative to one another. This state is known as sticking. The slip calculation determines when a point transitions form sticking to slipping. Hard contact pressure over-closure method is enforced to define the normal behavior of the contact between the two surfaces. It essentially means that there is no contact pressure transmitted unless the two surfaces are in contact. It also restricts the finite element mesh of HC(master surface) to penetrate the piston(slave surface) surface mesh.

3.3.4 Dynamic Analysis

In this study, as the movement of the structure is dependent on the inertia of the body, an implicit dynamic analysis was carried out to evaluate the dynamic response of the multi-body. The choice of the analysis is further supported by the considering the length of time for which the response is recorded. At each step global mass and stiffness matrices are assembled and inverted to solve force and moment equilibrium equations. Even though each step is computationally expensive the analysis is unconditionally stable. A semi-discrete equation of motion is a second order ordinary differential equation that can be written as,

$$M\ddot{d} + C\dot{d} + Kd = F \tag{3.23}$$

Here M is the mass matrix, C is the viscous damping matrix, K is the stiffness matrix, F is the external load vector and $\ddot{d}$ is the acceleration, $\dot{d}$ is the velocity and d is the displacement. M, C and K are symmetric matrices and M is positive definite whereas C and K are positive semi-definite. A widely used numerical incremental scheme in structural multibody dynamics is the Newark method [45]. In this method the displacement and velocity is determined as,

$$d_{n+1} = d_n + \Delta t v_n + \frac{\Delta t^2}{2}[(1-2\beta)a_n + 2\beta a_{n+1}] \tag{3.24}$$

$$v_{n+1} = v_n + \Delta t[(1-\gamma)a_n + \gamma a_{n+1}] \tag{3.25}$$

Here, n represents the increment. Δt denotes the time increment and d_n,v_n and a_n are approximations of $d(t_n)$, $\dot{d}(t_n)$ and $\ddot{d}(t_n)$ respectively. The parameters β and γ are numerical damping parameters that determine the stability and accuracy of the numerical scheme. Using equations 3.24 and 3.25 the semi-discrete equation of motion is discretized in time as,

$$M\ddot{d}_{n+1} + C\dot{d}_{n+1} + Kd_{n+1} = F_{n+1} \tag{3.26}$$

A more general implicit scheme is introduced in Hilber-Hughes-Taylor - α method [46] and implemented in Abaqus. In this method a factor α is introduced to increase the damping for transient problems without degrading the order of accuracy. It is second order accurate and allows energy dissipation to stabilize the numerical scheme. Introducing the numerical damping parameter α in equation 3.28 it can be modified as,

$$M\ddot{d}_{n+1} + (1+\alpha)C\dot{d}_{n+1} - \alpha C\dot{d}_n + (1+\alpha)Kd_{n+1} - \alpha Kd_n = F_{\bar{t}_{n+1}} \tag{3.27}$$

where,

$$\bar{t}_{n+1} = t_n + (1+\alpha)h \tag{3.28}$$

Lesser the value of alpha more is the numerical damping in the scheme. In this study of multibody dynamics system a moderate dissipation was chosen to stabilize

the time integration scheme. The parameters chosen for the simulations are given in table 3.2.

Table 3.2: HHT-α method parameters [3]

Parameter	Value
α	-0.414214
β	0.50000
γ	0.914214

3.3.5 Load and Boundary Conditions

A buoy that is connected to the tip of the floater's arm, not shown here, experiences the hydrodynamic forces. In this study, it is assumed that the load endured by the buoy is directly transferred to the floater arm tip, at the zone where it is connected to the arm. The scaled forces in figure 2.2 is applied to the floater arm tip as shown in figure 3.1. This is done by importing the force data to the Abaqus load module. Additionally, the bracket that is used to hold the HC is fixed at its base. The lower surface of the bracket is constrained in all degrees of freedom. Moreover, to accurately model the translator joint along the axis of HC and piston one end of the connector was constrained in all degrees of freedom. In figure 3.1, P represents the applied load whereas the angle θ is the angle made by floater's arm with the horizontal axis.

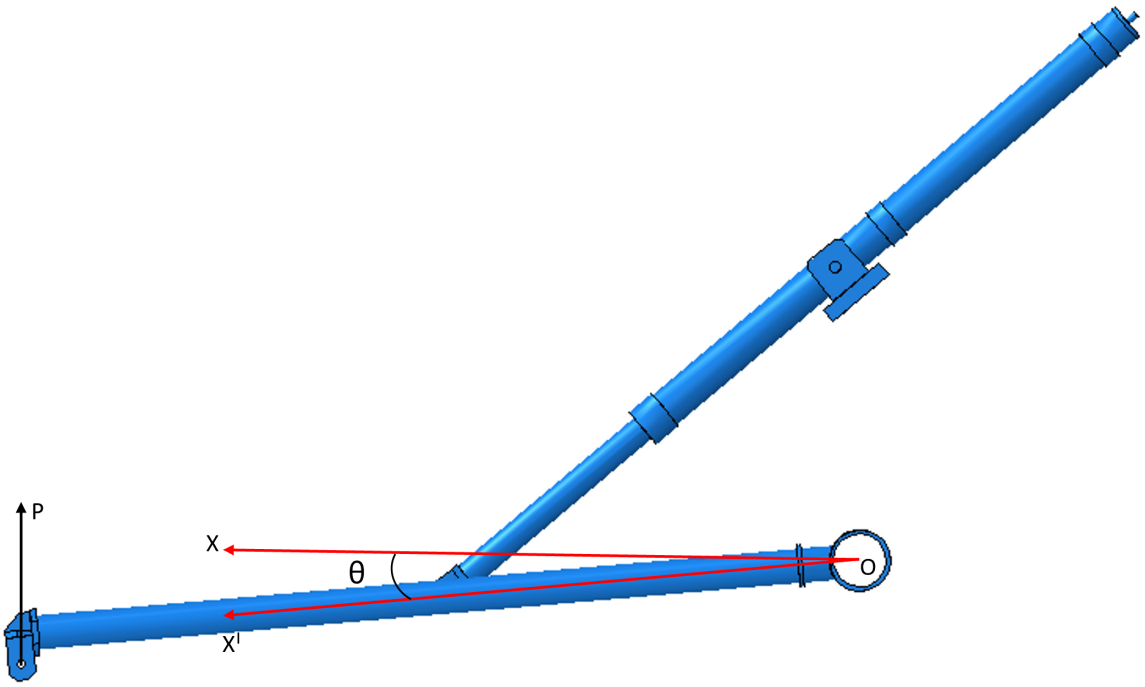

Figure 3.1: Load applied to arm tip.

3.3.6 Finite Element Mesh

As discussed earlier in FEM the domain is discretized using FEs. This process, in general, is known as meshing. Abaqus provides the flexibility to choose the type of element used to mesh the domain depending on the type of analysis. For instance, it categorizes 3D Stress element family for analysis involving stress, heat transfer family for analysis that is dependent on temperature. In regards to the geometry of element for the three-dimensional domain, the element type is tetrahedral, wedges and hexahedral(brick) in shape. Additionally, this element can either be linear or quadratic which implies that approximation between two consecutive nodes will be carried out linearly or quadratically. The primary advantage of tetrahedral elements is that it can easily mesh complex geometry. The drawback of using this is that the results may not be accurate. However, the error can be minimized by using a quadratic element and increasing the number of elements to a finer mesh. However, the number of elements should be optimized as increasing the number of elements increases the computational

time. On the other hand, hexahedral structured mesh provides accurate results, and because less number of elements will be required to mesh the same volume, it reduces the computational cost. In this study, the arm, because of its intricate geometry, is meshed with 10-node quadratic tetrahedron element. Whereas, HC, piston, and bracket are meshed using 8-node linear brick with reduced integration and hourglass control. The motivation behind using reduced integration instead of full integration is to reduce the computational cost. It is reduced by 30% when 8 Gaussian quadrature points in reduced integration points are used instead of 27 as in full integration [3].

Table 3.3: Mesh properties.

Part	Element type	Global mesh size(m)	Number of elements
Arm	Tetrahedral(C3D10)	0.012	126231
Piston	Brick(C3D8R)	0.008	12434
HC	Brick(C3D8R)	0.008	21546
Bracket	Brick(C3D8R)	0.008	10527

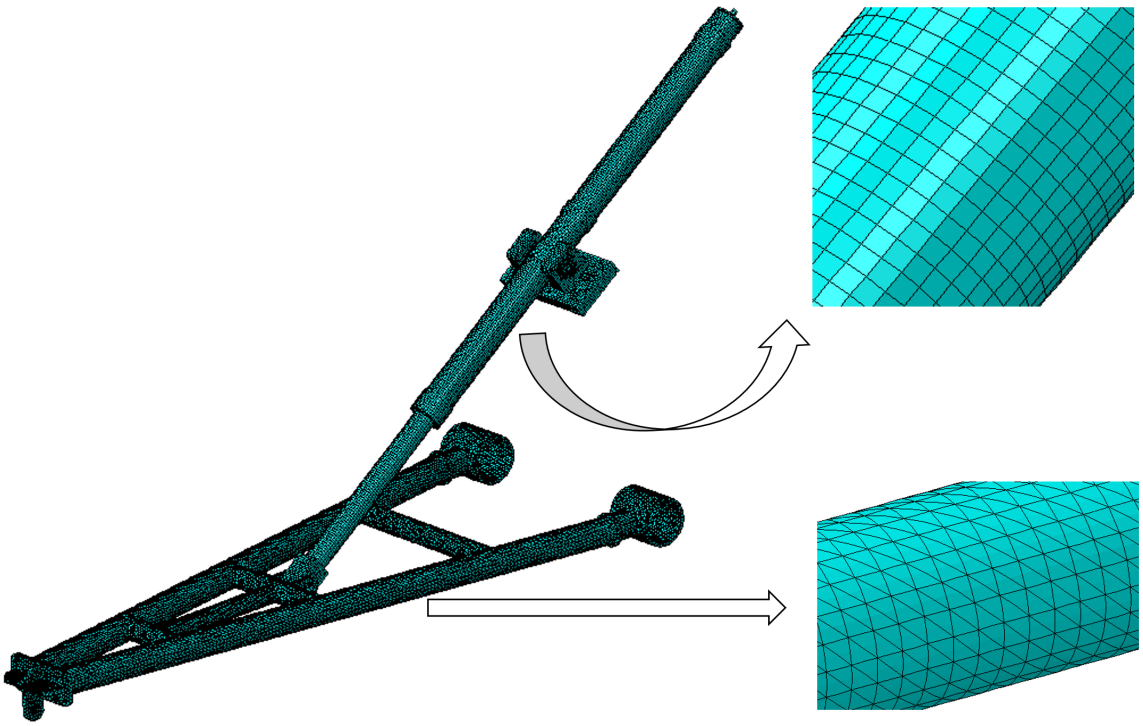

Figure 3.2: Finite Element Mesh.

CHAPTER 4: RESULTS

The scaled force in chapter 2 was applied to the floater arm tip. Here, the force acts as a natural boundary condition. The force on the arm pushes the arm in the direction of the force thus forcing the piston to translate along HC and HC to rotate through the axis of rotation. The displacement and velocity variation of arm tip is noted. It shows the cyclic behavior as that of the force applied. Furthermore, the force on the arm gives rise to deformation and stresses on all the WEC parts. The validation is performed in two fold. First the displacement of floater arm is compared with the displacement form the literature. Secondly, the effect of PTO damping on floater arm displacement and velocity is compared with an experimental study.

4.1 Validation cases

4.1.1 Displacement of floater arm

The displacement and velocity show the similar heaving motion as from the work done by Lin et al. [44]. The displacement shows a good agreement even-though the magnitude of velocity in this study is found to be large. This is because in this study the period of force is taken to be 1 second whereas by Lin it is 6.2 seconds. Because of which the arm has to travel the same distance in a shorter period which means that it has to have higher velocity. The displacement of the arm is shown in figure 4.1.In addition to that, dimensions of the WEC are also different, and the joints were explicitly modeled in the Abaqus the properties of which affect the overall behavior of the WEC. Furthermore, as discussed in the later section the angle of the floater's arm also affects the movement of the arm.

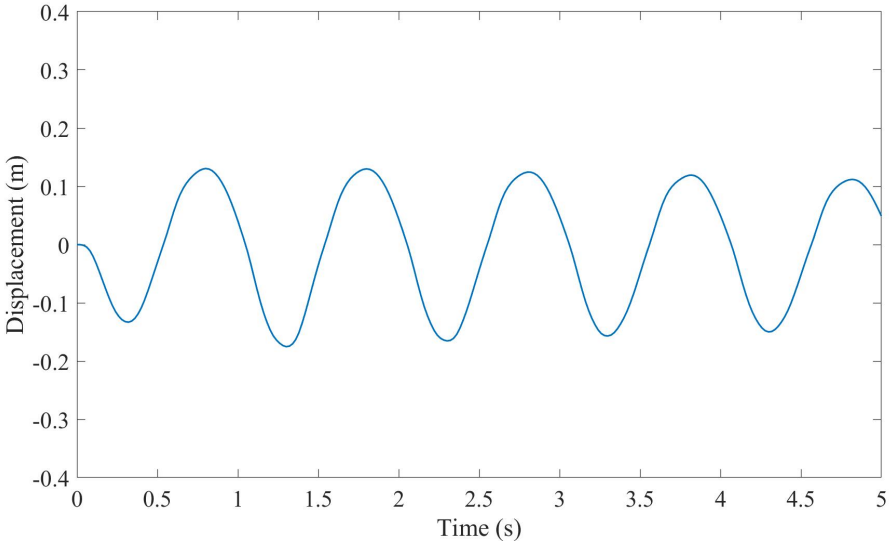

Figure 4.1: Validation case

4.1.2 Effect of Damping

In a recent experimental work by Zang et al. [26] the effect of PTO damping on the displacement and velocity was considered. Even though the model of WEC varies the PTO system in both the studies are similar, a linear hydraulic system. The experiments showed that the amplitude of displacement, as well as velocity, decreases with the increase in the damping of PTO. Moreover, the phase difference between the load and displacement increases with the increase in damping. A similar trend was observed in this study and is shown in figure 4.2.

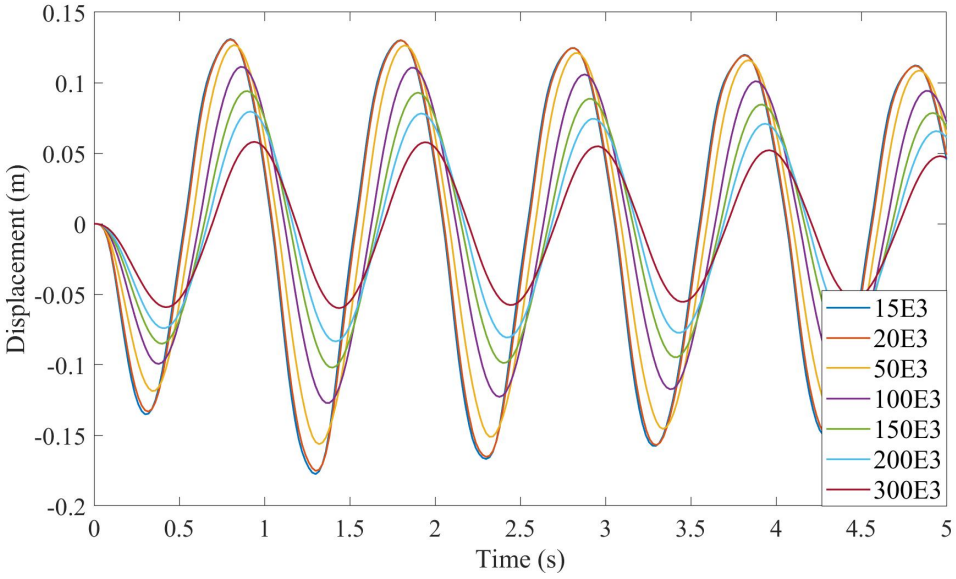

(a)

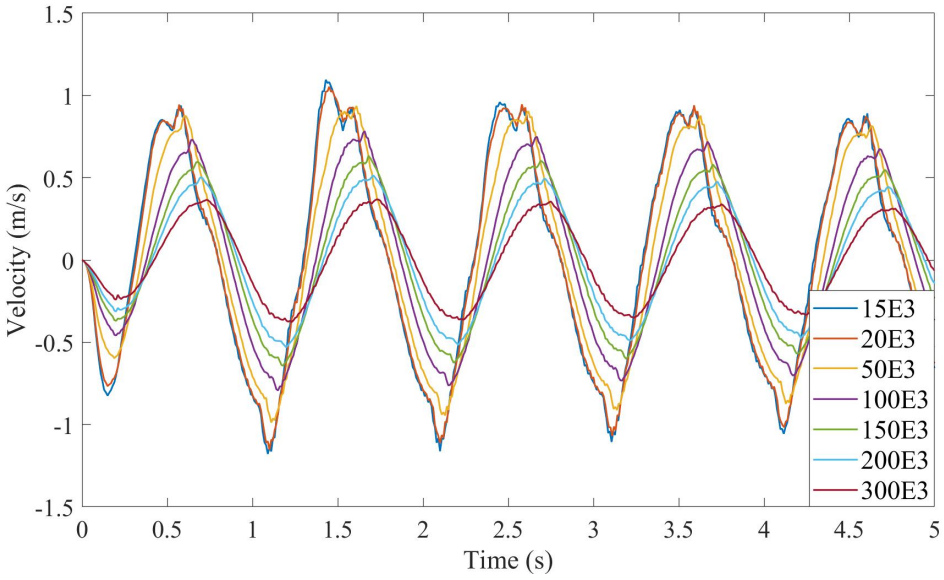

(b)

Figure 4.2: Displacement and Velocity of arm with increasing PTO damping $(N/(m/s))$.

4.2 Stress And Deformation

4.2.1 Mesh Sensitivity Analysis

As discussed earlier the spatial domain of the structure is discretized into a finite number of elements. However, the result of displacement and stress changes with the number of elements used. In general, the results get more accurate as we use more and the number of elements with finer meshes. As the mesh gets finer, it behaves more like a continuous structure, and the approximate solution gets closer to the actual solution. The discrepancy in results is because discrete elements are used to model a continuous structure and having a coarser mesh may not capture the property under investigation. That being said, increasing number of elements increases not only the computational cost but also the memory needed to store the data. To counter this issue mesh independence study needs to be done to find a good enough mesh size for a reasonably accurate result.

In this study, a convergence test was first carried out to find a suitable mesh size. Various mesh sizes from 0.025m, 0.02m, 0.014m, 0.012m was taken into consideration. For initial analysis, a full cycle load was applied for 1 second, and the simulations were run on UNC Charlotte Copperhead cluster. 1 node and 16 processors were utilized for the analysis. As shown in figure 4.3 the maximum stress increases with the decrease in mesh size but it converges at a mesh size of 0.012 m. Henceforth, the mesh size of 0.012 m was chosen for the simulations. The simulation time for 1 second of the load was around 40 minutes.

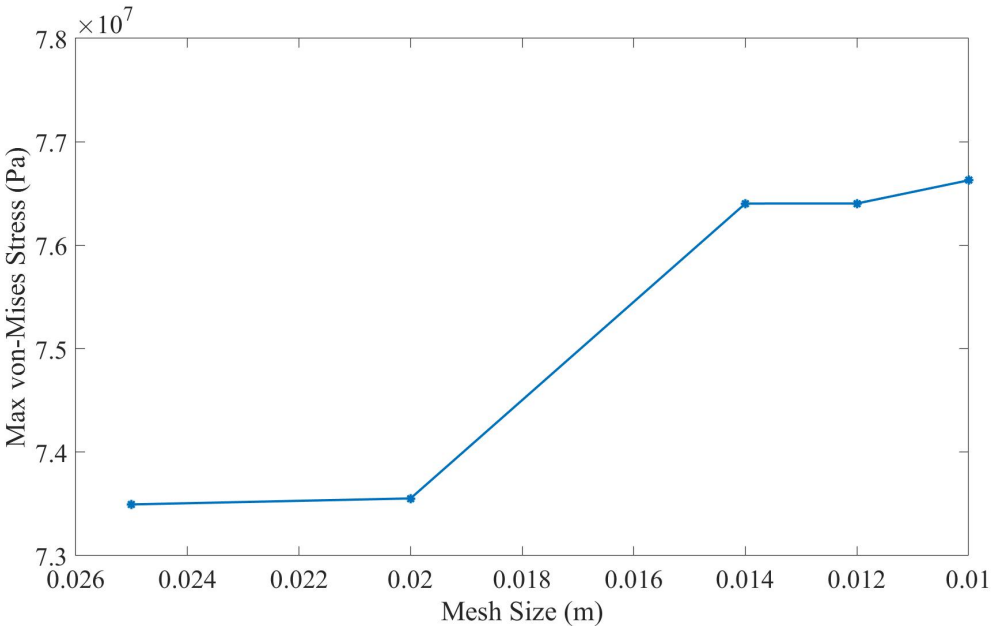

(a)

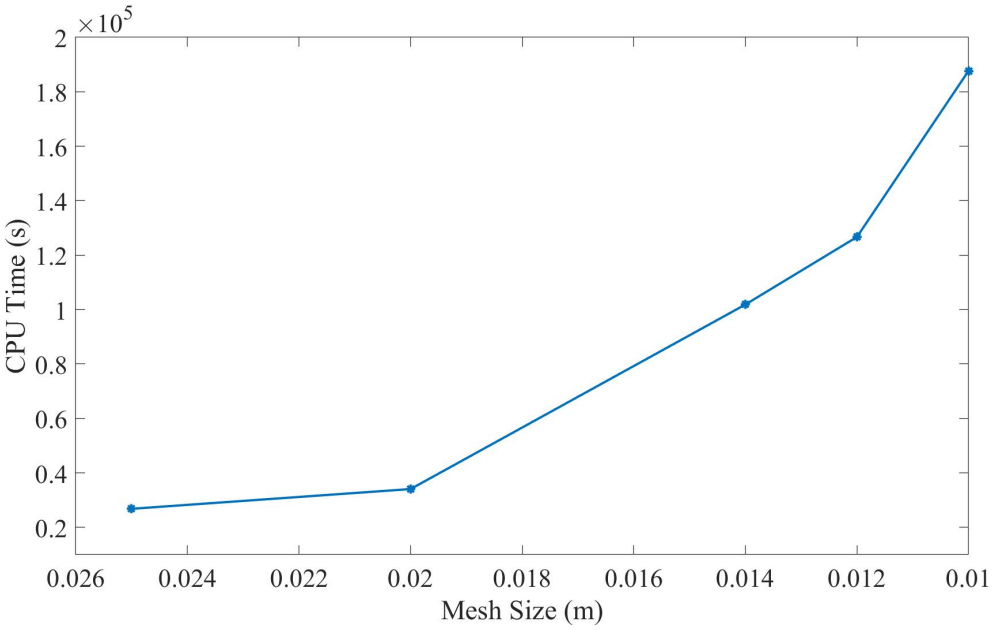

(b)

Figure 4.3: Mesh Convergence Analysis.

4.2.2 Stresses on WEC parts

The scaled forces obtained as shown in figure 2.2 was applied to the arm tip to determine the cross-section area (CSA) with maximum cyclic stress. The subsequent stresses analysis was carried out at a floater arm angle of 2.5^o and damping of 20000 $N/(m/s)$ for the PTO system.

4.2.2.1 Bracket

The stress distribution in the bracket at maximum load is shown in figure 4.4. While the stress concentration in the bracket lies in the area where it holds the hydraulic cylinder however the cyclic stresses are maximum on the outer edges of the bracket. The von-Mises stress at the various cross-sectional area of the bracket is shown in figure 4.5. It is observed that the stress in minimum at the center CSA and increases as we go further from the center. Additionally, the maximum stress is less than the yield stress of the material thus only elastic deformation will occur.

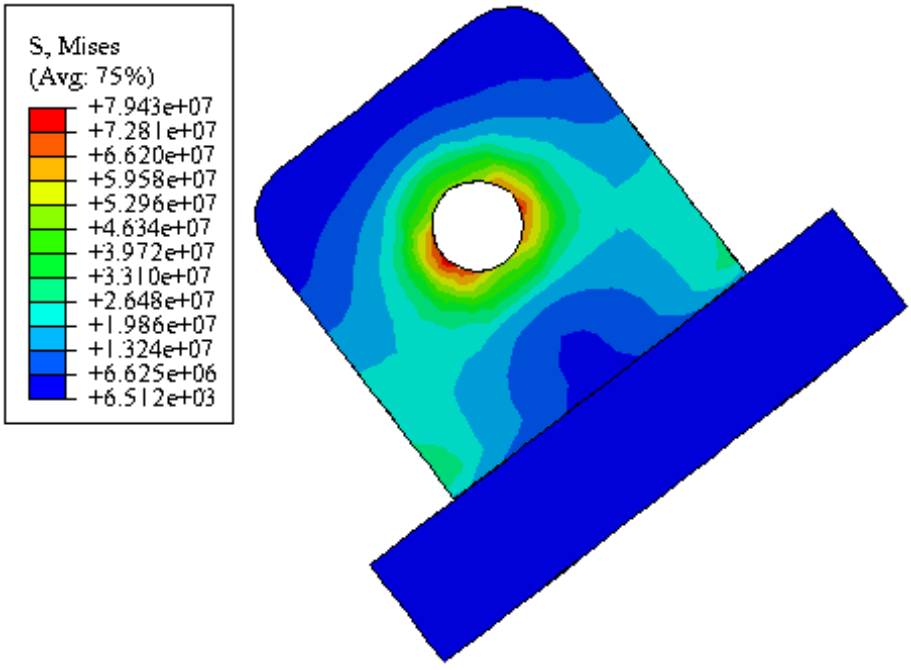

Figure 4.4: Stress distribution in Bracket.

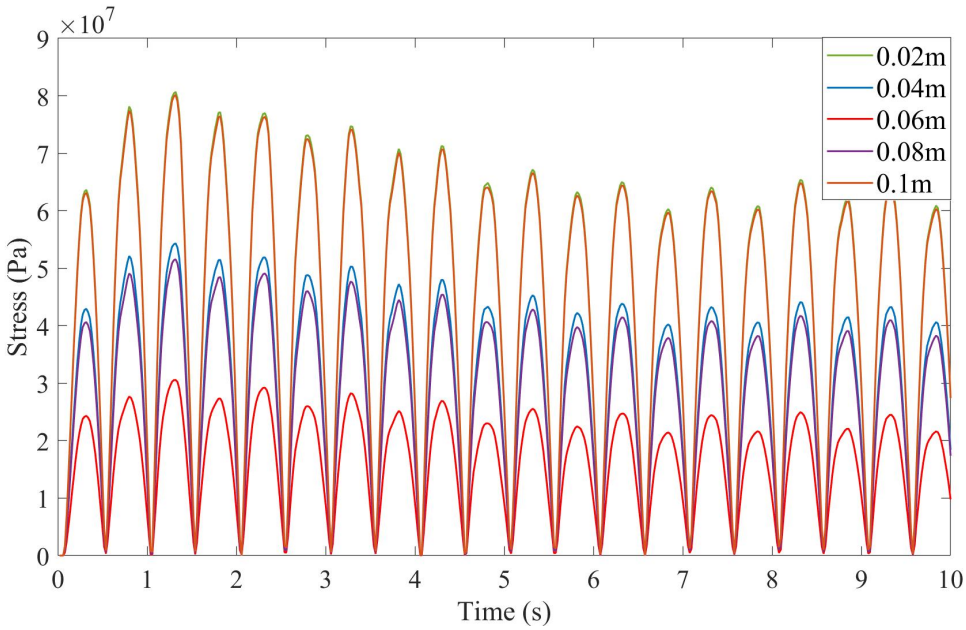

Figure 4.5: Stress of bracket at various cross-sections.

4.2.2.2 Hydraulic Cylinder

The stress distribution in the HC is shown in figure 4.6. Similar, to the case of the bracket the stress concentration lies near the hinge connection between the two parts. The stress at various CSA of HC is shown in figure 4.7. The CSAs were taken from left most end the HC. The maximum stress in HC increases as we get closer to the axis of rotation. However, the increase is not very significant whereas as we go further right side from the hinge connection, the stress decreases.

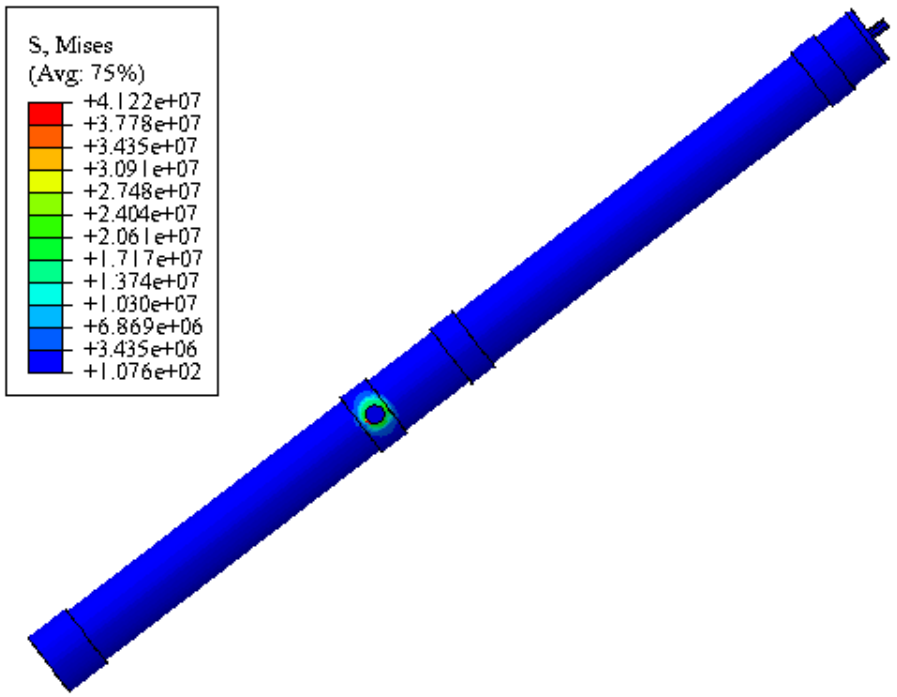

Figure 4.6: Stress distribution in HC

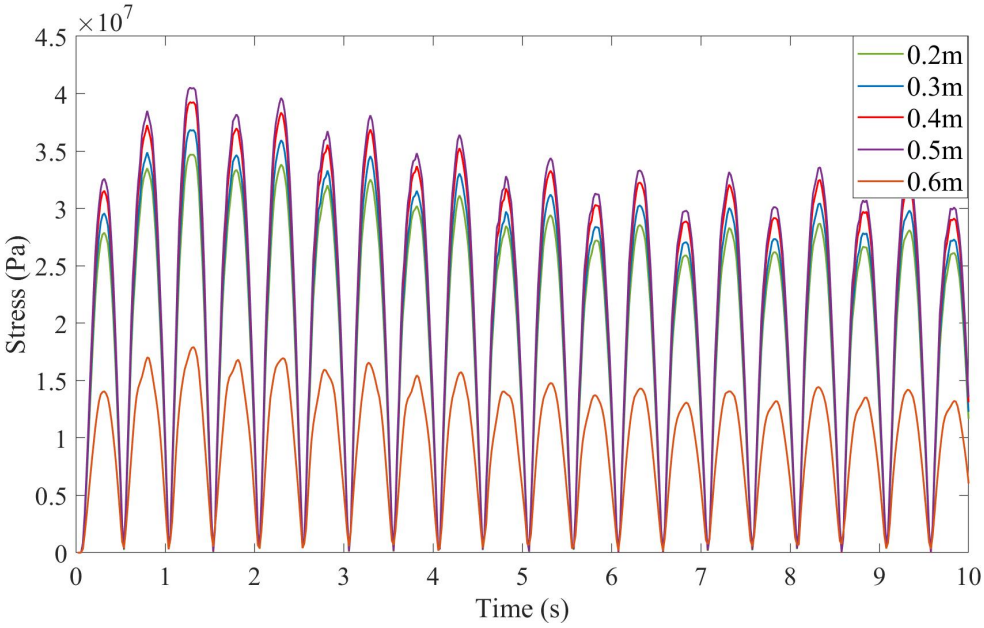

Figure 4.7: Stress of HC at various cross-sections.

4.2.2.3 Piston

As a part of the PTO system piston transmits the forces endured by the arm to the HC for energy conversion. The stress distribution in the piston is shown in figure 4.8. The contact between the inner surface of HC and the outer surface of the piston creates a normal force on the piston surface as the piston slides into HC. Because of which stress is higher at the region where it is in contact with the HC. The stress at various CSA of the piston is shown in figure 4.9. Similar, to the case of HC the CSAs are taken from left most end of the piston. The maximum stress gradually increases along the length of the piston.

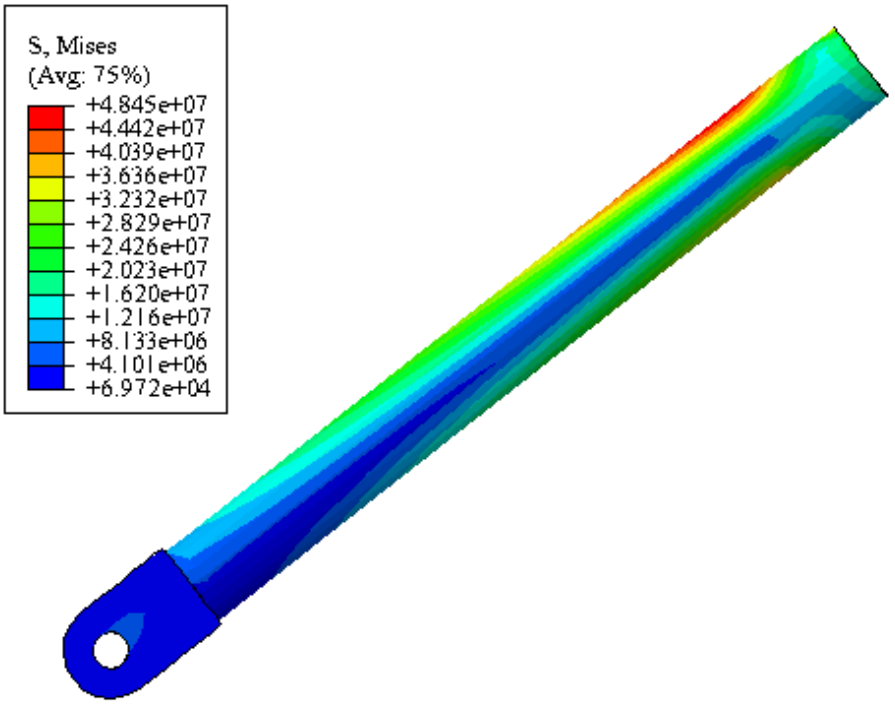

Figure 4.8: Stress distribution in Piston.

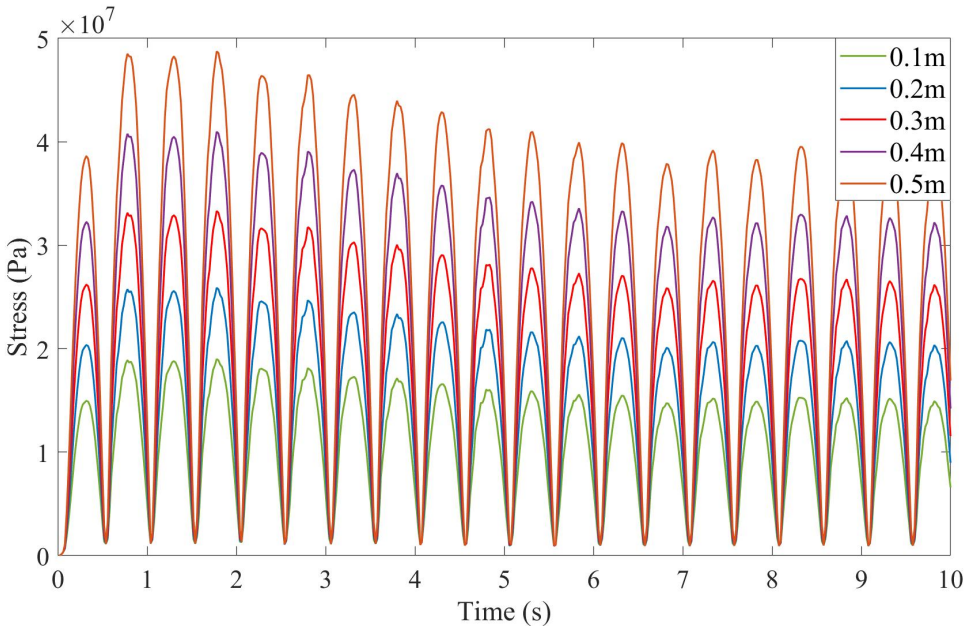

Figure 4.9: Stress of piston at various cross-sections.

4.2.2.4 Arm

The maximum stress for arm lies near the area where it is connected to the piston as shown in figure 4.10. It is attributed to the resistance of the piston movement caused by the PTO damping. Moreover, this resistance causes the arm to bend near this area leading to higher stress. In addition to that, the stress near the float region is lower because of the hinge connection on the other end of the arm that allows it to rotate. Figure 4.11 shows the von-Mises stress for the floater arm at various CSAs. The cross-section distances were taken from the floater side of the arm. All the regions show a periodic behavior of stress with maximum stress to be close to 34 MPa at maximum load.

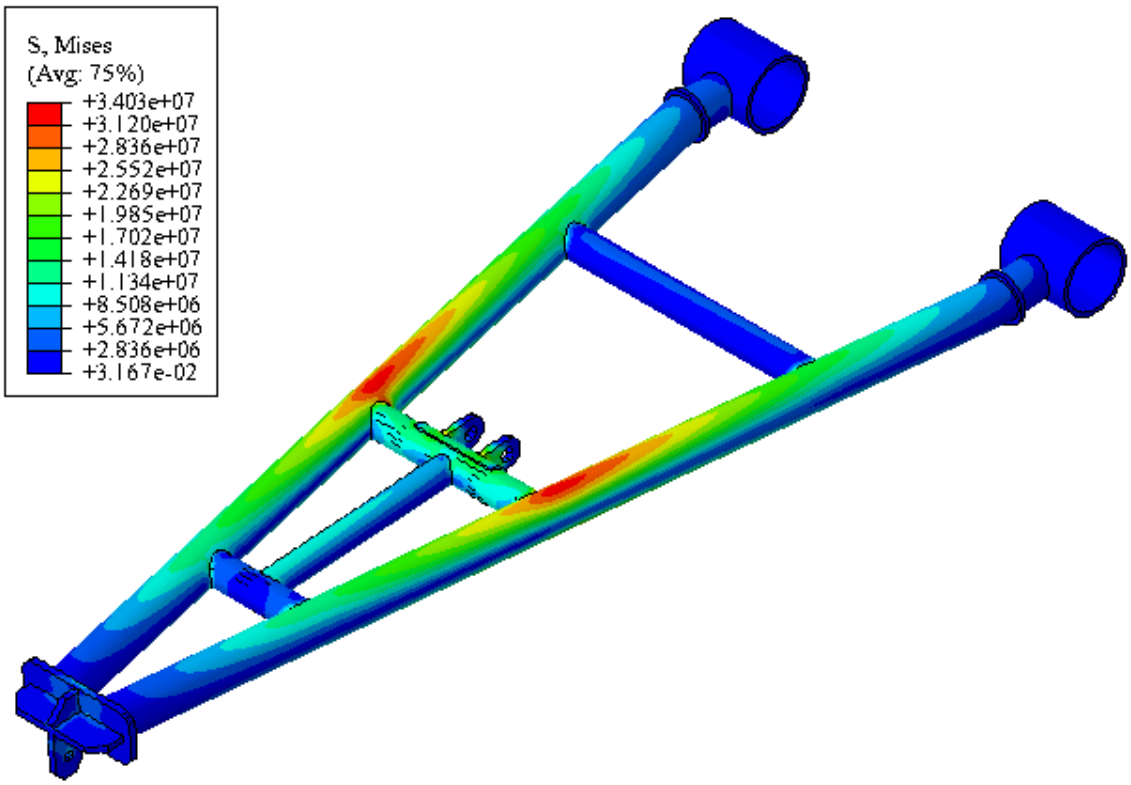

Figure 4.10: Stress distribution in Arm.

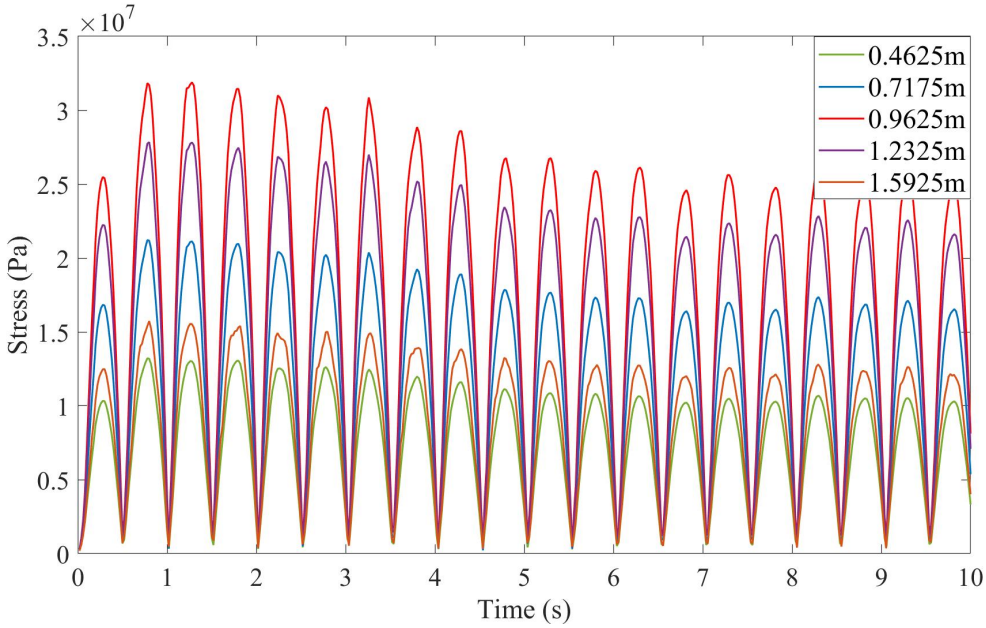

Figure 4.11: Stress of arm at various cross-sections.

The cross-sectional area for each part that has the maximum von-Mises stress is considered and is shown in figure 4.12. The maximum stress is found to be on the bracket (79.4 MPa) with gradually decreasing from the piston (48.45 MPa), HC (41.2 MPa) to arm (34.03 MPa). None of the WEC parts experience yielding or plastic deformation as the maximum stress for each case is considerably below the yield strength of the material, 355 MPa. However, the stress does show a periodic behavior which will lead to fatigue damage as shown in the later section.

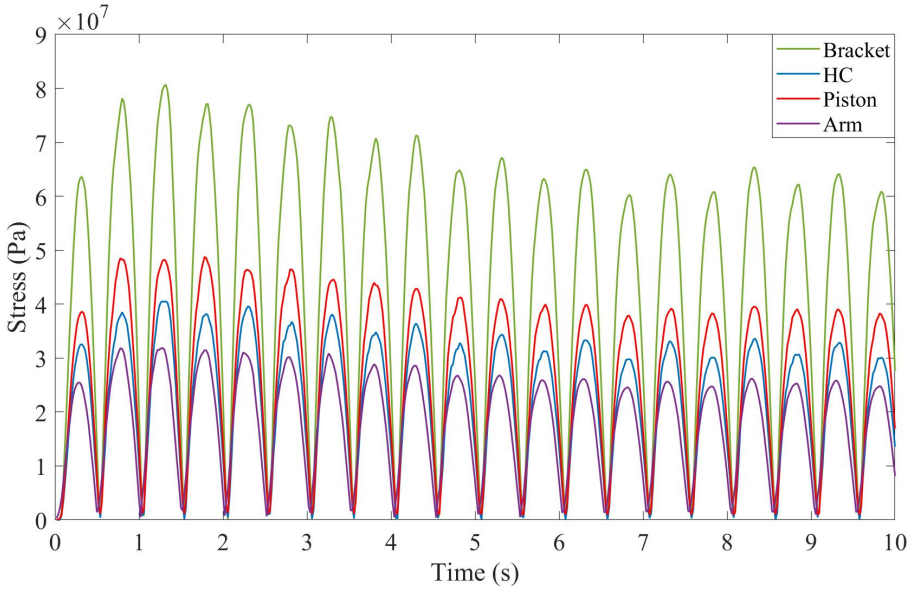

Figure 4.12: Maximum von-Mises stress on all the WEC parts.

4.2.3 Deformation

The deformation in all the parts at 1.3 s, maximum negative load, is shown in the figure 4.14, with the original configuration at no load for reference. It is observed that the maximum deformation occurs nears the floater arm tip. Additionally, the bracket has minimum deformation and piston and HC being in the intermediate range. Furthermore, the deformation in the parts has a periodic nature with the maximum being in the arm, 0.1796 m, as shown in figure 4.15. Moreover, the periodic deformation has a decreasing trend from piston 0.0874m, HC 0.01767 m and minimum to be in the bracket of around 10E-3 m.

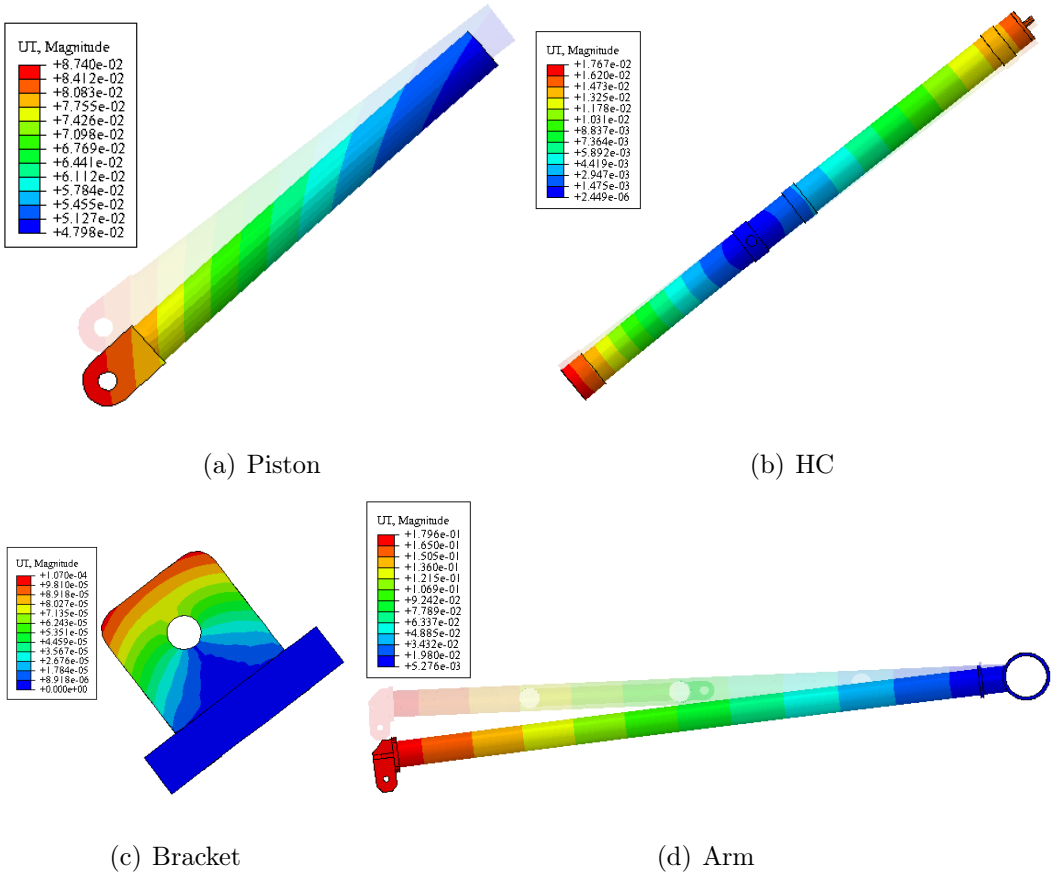

(a) Piston (b) HC

(c) Bracket (d) Arm

Figure 4.13: Deformation in WEC parts

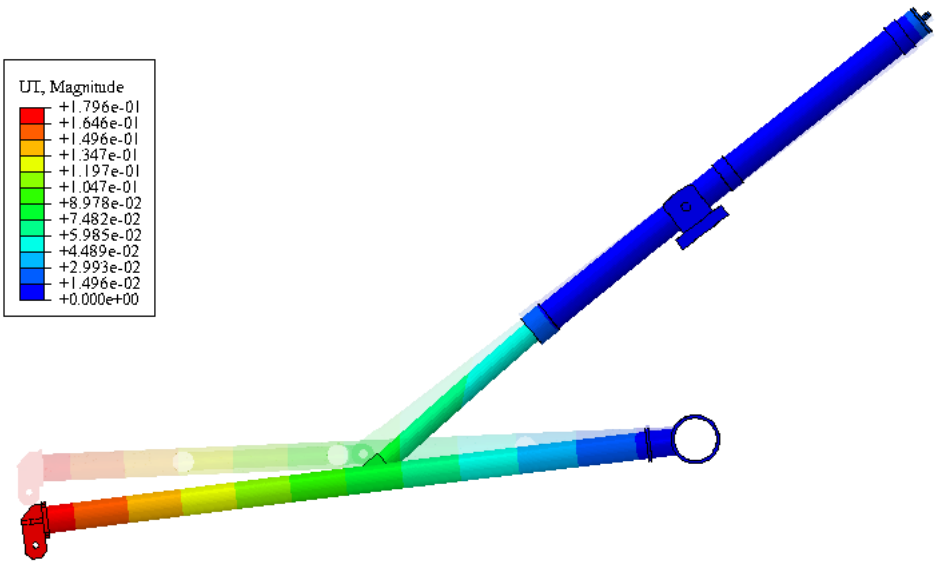

Figure 4.14: Deformation in WEC

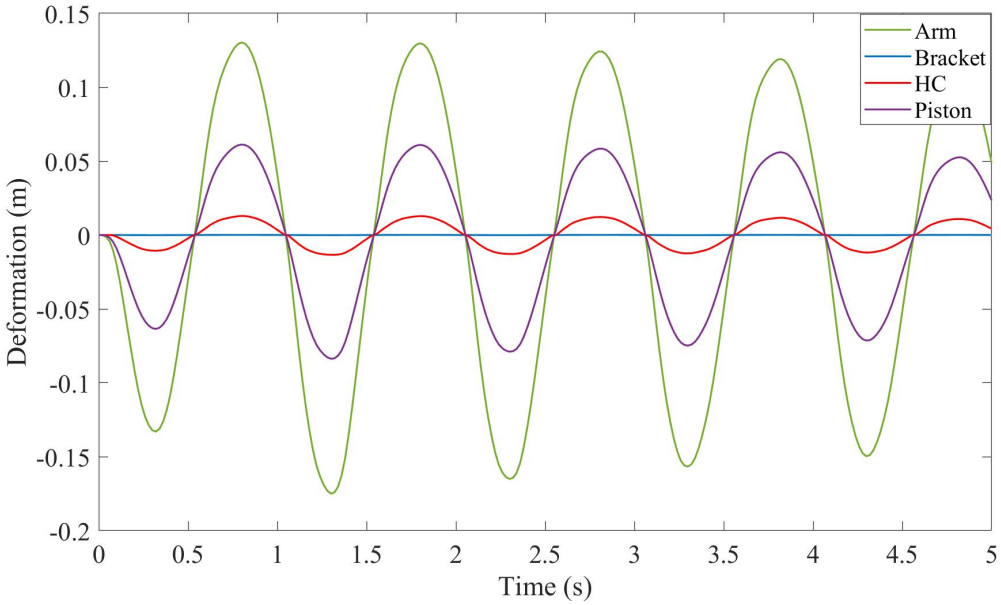

Figure 4.15: Deformation in WEC parts

4.3 Parametric study

4.3.1 Damping

PTO systems are the characteristics of a WEC. In this study, the PTO consists of the piston and HC. Hydraulic fluid inside the HC offers to damp to the system. In this section, the effect of damping is studied on the stress on WEC parts. Damping coefficients from a range of 20000 $N/(m/s)$ to 300000 $N/(m/s)$ is considered. It is found that the maximum stresses on the piston, HC and bracket decreases with the increase in damping. However, there is also an increase in lag between the stresses of the arm and all the other parts as shown in figure 4.16. This lag is because of the delay in response offered because of the damping.

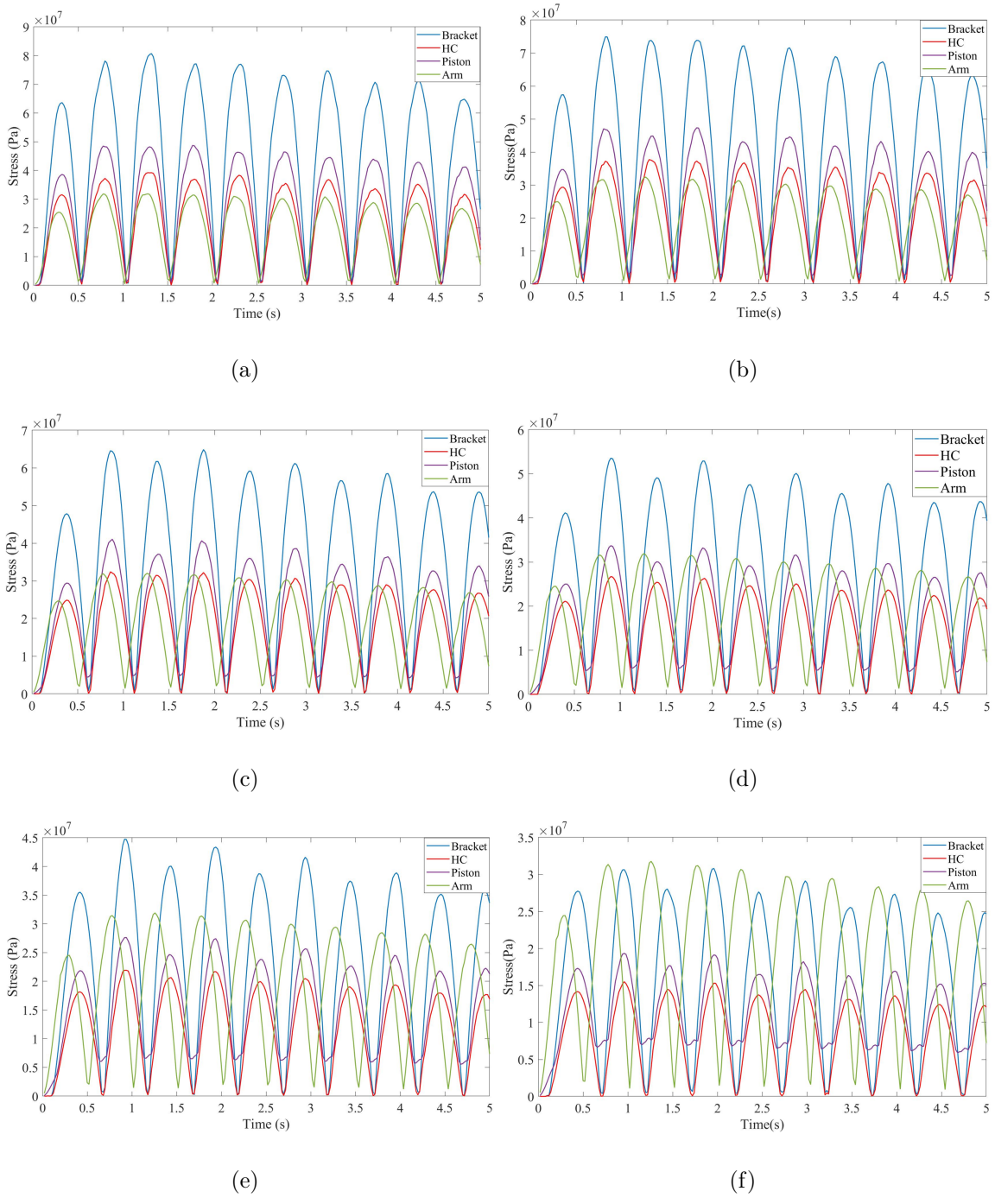

Figure 4.16: Stress of WEC parts with increasing damping, (a) 20000 $N/(m/s)$, (b) 50000 $N/(m/s)$, (c) 100000 $N/(m/s)$, (d) 150000 $N/(m/s)$, (e) 200000 $N/(m/s)$, (e) 300000 $N/(m/s)$).

4.3.2 Angle

In this section, the effect of floater's arm angle $'\theta'$ was studied. It was found that the magnitude of displacement decreases by 18.33% as the angle increased from 0^o to 20^o. The velocity also decreases with the increase in the angle from 0^o to 20^o by 13.33%. This is due to the decrease in resultant force in a vertical direction acting on the arm as the angle increases.

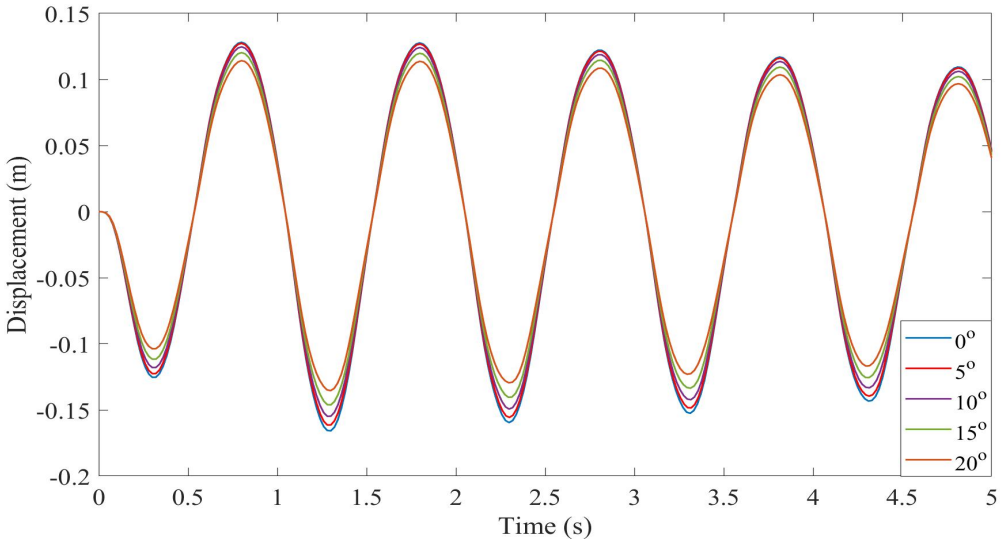

Figure 4.17: Displacement of Arm with increasing angle of arm

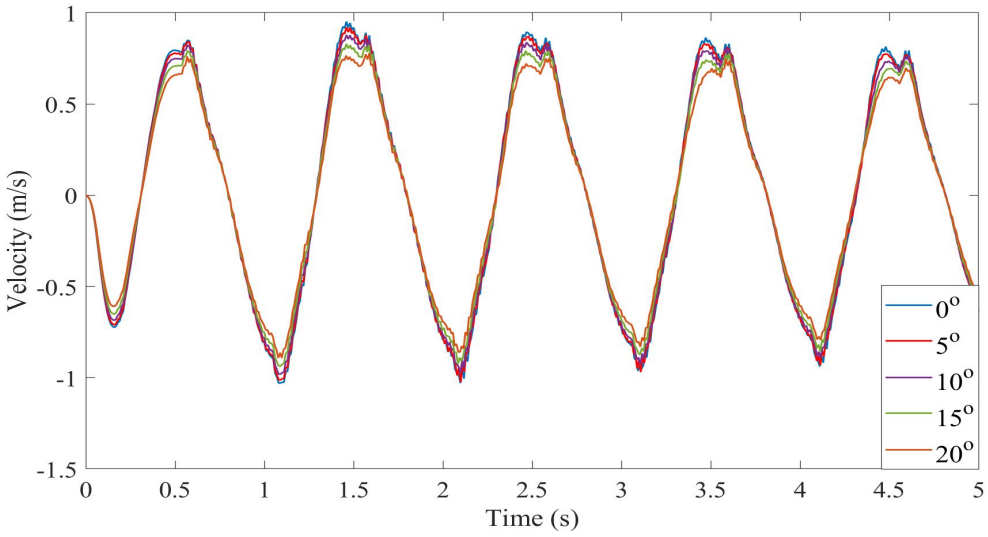

Figure 4.18: Velocity of Arm with increasing angle of arm

The stresses on all the parts decrease with the increase in floater's arm; however, for a given damping coefficient there is no lag between the stress.

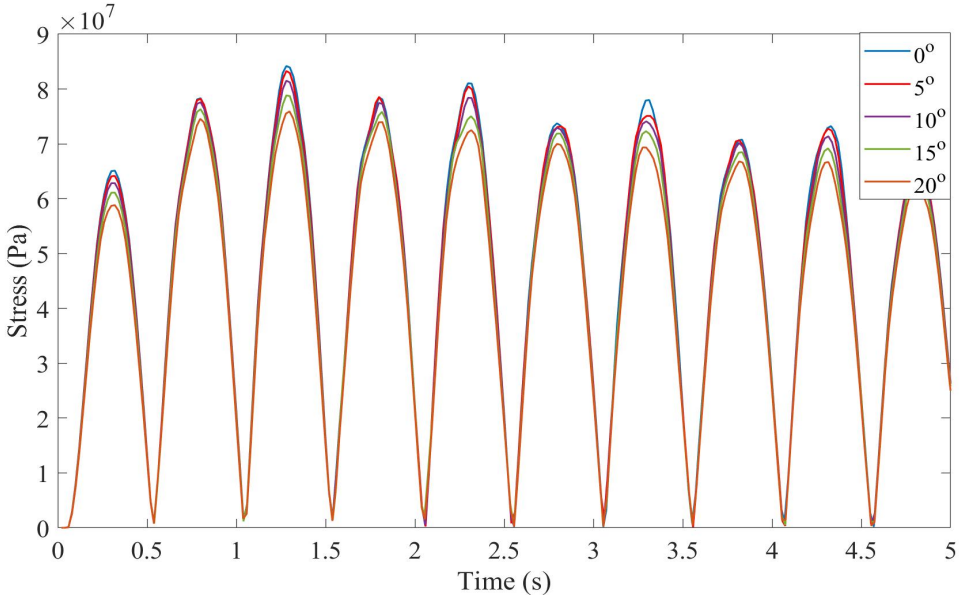

Figure 4.19: Stress of bracket with increasing angle

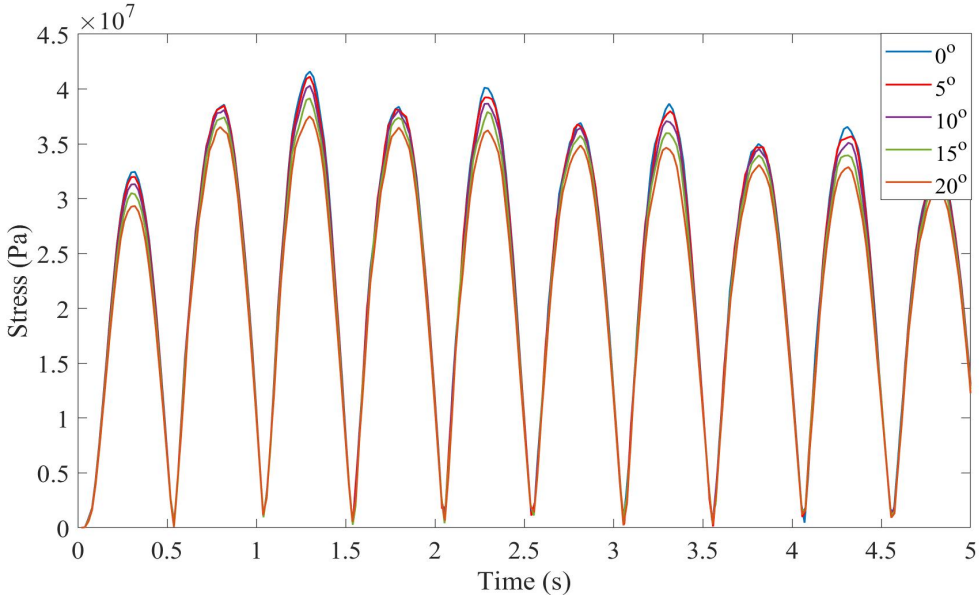

Figure 4.20: Stress of HC with increasing angle

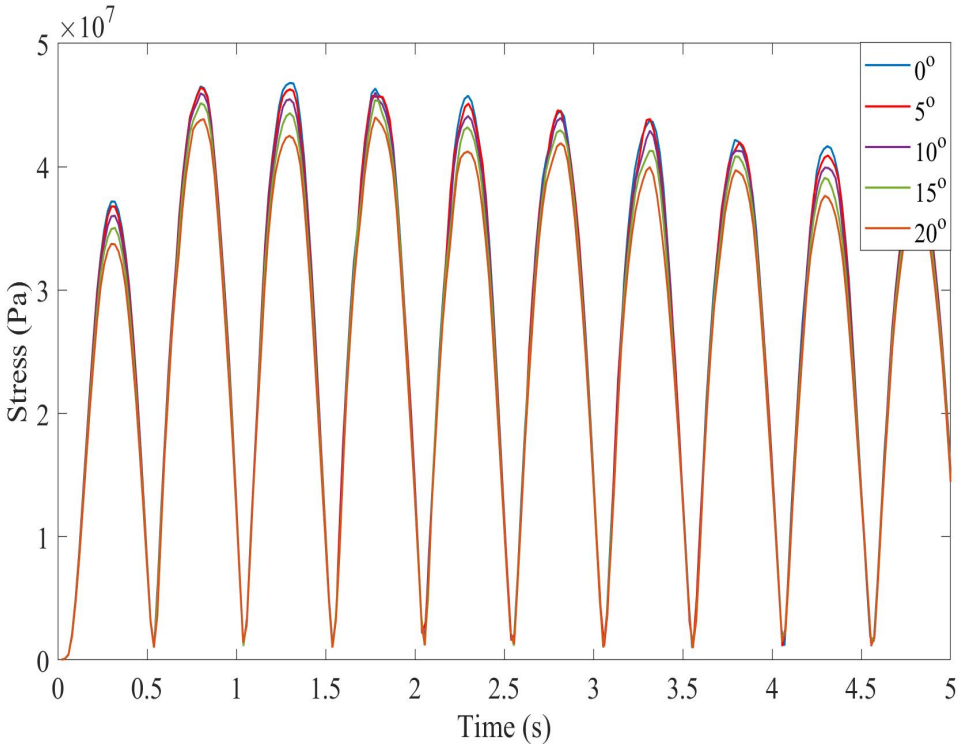

Figure 4.21: Stress of piston with increasing angle

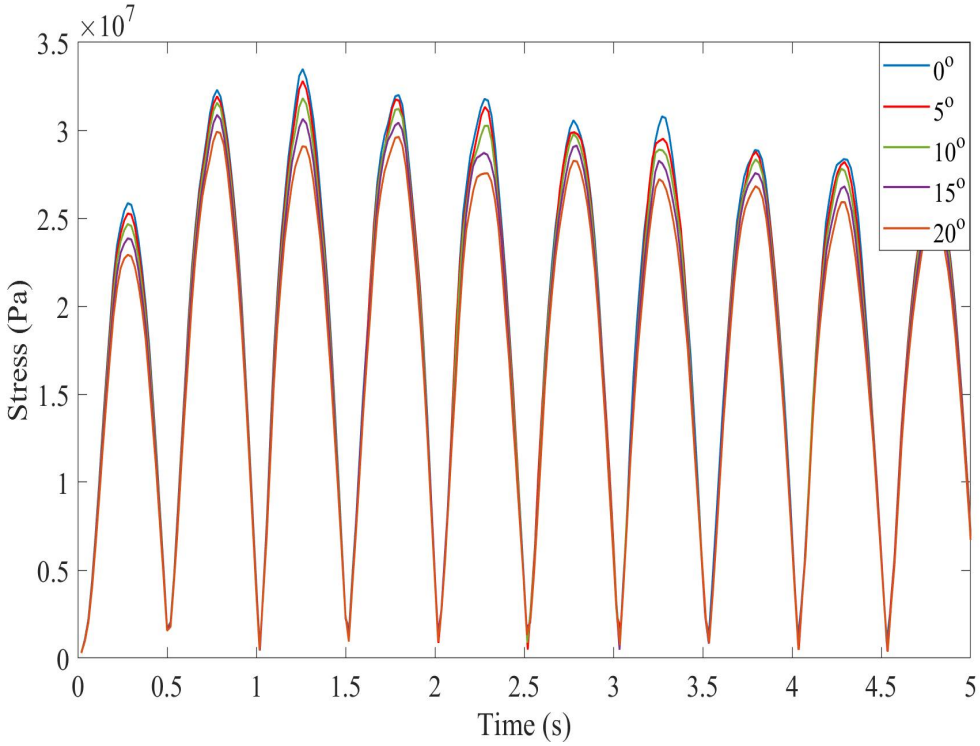

Figure 4.22: Stress of arm with increasing angle

4.4 Fatigue Life Assessment

The deformation and stress obtained show cyclic behavior. The cyclic loading leads to localized damage known as fatigue. This localized damage initiates plastic deformation initiating a crack near the region. The crack increases with the increase in the number of stress cycles causing the component to fail permanently. This makes fatigue life assessment important and necessary.

In this study, the well established S-N curve technique is used to determine the fatigue life of WEC parts that have the highest CSA of cyclic stress. The basic design for the number of cycles is given as [47],

$$\log N = \log \bar{a} - m \log \Delta\sigma \tag{4.1}$$

where N is the predicted number of cycles to failure for a stress range $\Delta\sigma$, $\bar{a}$ is the intercept on $logN$-axis by the S-N curve, m is the negative inverse slope of S-N curve. The intercept and slope are defined with respect to the number of cycles the WEC needs to undergo before failing and the environment. The intercept and slope for the whole assembly (i.e., located out of the water) are taken to be 12.592 and 3, respectively [47]. Additionally, the range of signed von-Mises stress is taken into consideration. Mises stress only captures the positive part of the stress cycle whereas signed von-Mises takes into account the negative part as well. In literature signed von-Mises stress is used as a governing factor for fatigue life [48]. The number of cycles that the WEC parts can withstand before failing is shown in figure. Here, the angle of floater arm is taken to be 2.5^o and PTO damping to be 3E5 $N/(m/s)$.

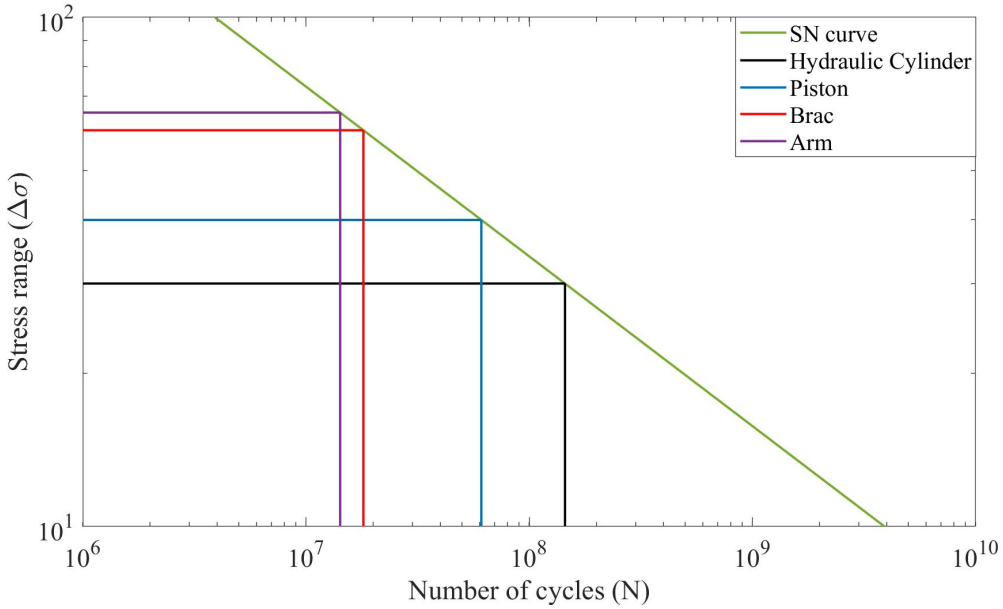

Figure 4.23: S-N curve

To obtain the fatigue life in years the time period for the waves is taken from the national weather service data [49]. In figure 4.24 the effect of PTO damping on fatigue life of each part is shown. It is observed that all the WEC parts show an increasing trend of fatigue life as the damping increases. The HC shows the maximum increase in fatigue life whereas there is a minimum change in fatigue of the arm with increasing damping. In case of changing arm angle as shown in figure 4.25 fatigue life in all the parts show an increasing trend with an increase in the floater's arm angle. A combination of PTO damping with arm angle can be used to increase the fatigue life of the WEC.

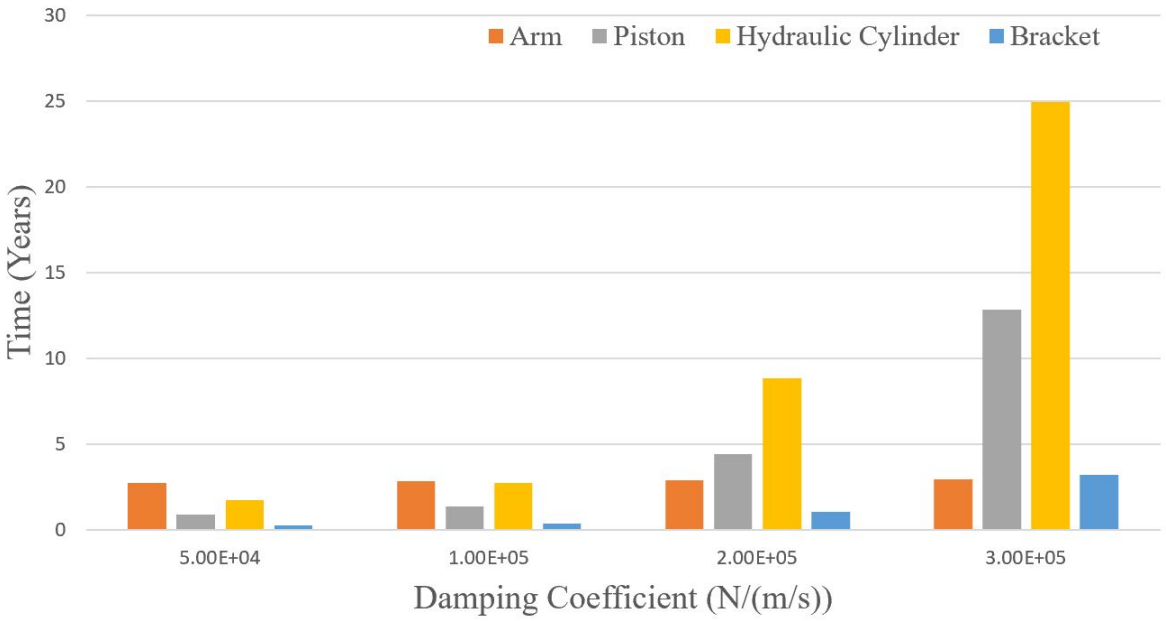

Figure 4.24: Effect of PTO damping on fatigue life

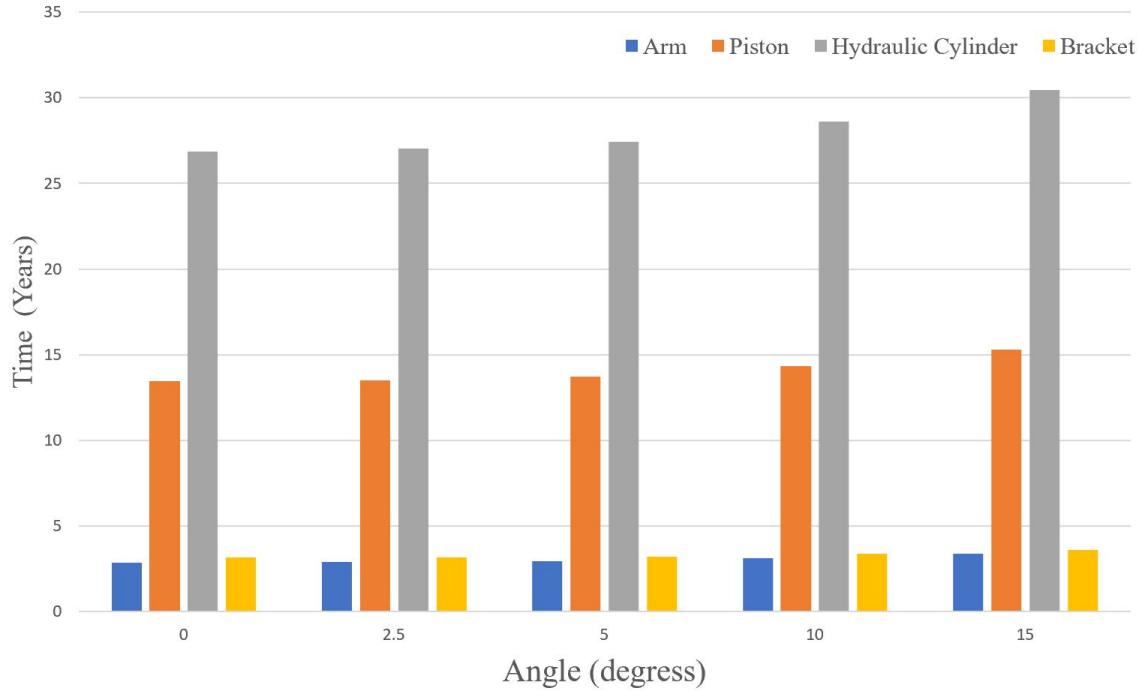

Figure 4.25: Effect of WEC arm angle on fatigue life

CHAPTER 5: CONCLUSIONS

In this study, a numerical analysis of a point-absorber wave energy converter was presented to calculate the stress and deformation on WEC parts. A linear elastic material constitutive model in combination with finite element method was used to model the dynamic behavior of the WEC. The forces due to ocean waves lead to stress on the WEC. The effect of PTO damping and arm angle on the displacement, velocity of the arm and more importantly the stresses was investigated. Furthermore, as the waves are periodic, which inevitably leads to fatigue failure, fatigue life of all the parts were determined. Following conclusions are drawn from the study:

1. There is a periodic variation in deformation and stress on all the WEC parts. Although the magnitude of stress is below elastic limit for the given material the cyclic nature of stress will lead to a fatigue failure.

2. PTO damping has a significant impact on the overall life and performance of the WEC. The stress on the WEC decreases with an increase in PTO damping. For a reasonable fatigue life the PTO damping should be atleast $3 \times 10^6 N/(m/s)$. For lower PTO damping floater arm has the highest life as compared to other parts but as the damping increases the floater arm life remains more or less consistent whereas as a significant increase in the life of piston, HC and bracket is observed. The increased damping decreases the maximum floater arm displacement which in turn reduces the stress on the piston, HC and bracket.

3. Increasing the floater arm angle decreases the maximum displacement of the arm. The results indicate that there is a decrease in maximum stress on all the parts which will increase the fatigue life of the WEC.

Renewable energy is the key to a sustainable future. The need for renewable energy demands a viable energy source. Ocean wave energy is considerably untapped and will be the emerging renewable source soon. The numerical model developed in this study can be used to model an optimized point-absorber WEC design to extract energy from the ocean waves. An array of the WEC presented in this study can be deployed offshore for a stabilized and maximized power output. In addition to that, the material selection process can be optimized by employing the numerical model for other material constitutive models.

REFERENCES

[1] H. Titah-Benbouzid and M. Benbouzid, "Ocean wave energy extraction: Up-to-date technologies review and evaluation," in *2014 International Power Electronics and Application Conference and Exposition*, pp. 338–342, IEEE, 2014.

[2] V. S. Neary, M. Lawson, M. Previsic, A. Copping, K. C. Hallett, A. LaBonte, J. Rieks, and D. Murray, "Methodology for design and economic analysis of marine energy conversion (mec) technologies.," tech. rep., Sandia National Lab.(SNL-NM), Albuquerque, NM (United States), 2014.

[3] *Abaqus 2017 documentation*.

[4] A. Subramanian, "Prediction of diffraction forces on a wave energy converter using bem and cfd approach," Master's thesis, The University of North Carolina at Charlotte, 2018.

[5] M. E. McCormick, *Ocean wave energy conversion*. Courier Corporation, 2013.

[6] M. Folley, T. Whittaker, M. Osterried, *et al.*, "The oscillating wave surge converter," in *The Fourteenth International Offshore and Polar Engineering Conference*, International Society of Offshore and Polar Engineers, 2004.

[7] T. K. Brekken, A. Von Jouanne, and H. Y. Han, "Ocean wave energy overview and research at oregon state university," in *2009 IEEE Power Electronics and Machines in Wind Applications*, pp. 1–7, IEEE, 2009.

[8] M. Melikoglu, "Current status and future of ocean energy sources: A global review," *Ocean Engineering*, vol. 148, pp. 563–573, 2018.

[9] G. Mork, S. Barstow, A. Kabuth, and M. T. Pontes, "Assessing the global wave energy potential," in *ASME 2010 29th International conference on ocean, offshore and arctic engineering*, pp. 447–454, American Society of Mechanical Engineers, 2010.

[10] D. Ross, *Power from the Waves*. Oxford University Press, USA, 1995.

[11] J. Leishman and G. Scobie, *The development of wave power: a techno-economic study*. Economic Assessment Unit, National Engineering Laboratory, Department of âŠ, 1978.

[12] Y. Masuda, "Wave-activated generator," *Int. Coll. on the Expositions of the Oceans (Trans.), Bordeaux, France*, 1971.

[13] S. H. Salter, "Wave power," *Nature*, vol. 249, no. 5459, pp. 720–724, 1974.

[14] R. Bedard, M. Previsic, G. Hagerman, B. Polagye, W. Musial, J. Klure, A. von Jouanne, U. Mathur, C. Collar, C. Hopper, *et al.*, "North american ocean energy statusâmarch 2007," *Electric Power Research Institute (EPRI) Tidal Power (TP)*, vol. 8, p. 17, 2007.

[15] M. Previsic, A. Moreno, R. Bedard, B. Polagye, C. Collar, D. Lockard, W. Toman, S. Skemp, S. Thornton, R. Paasch, *et al.*, "Hydrokinetic energy in the united statesâresources, challenges and opportunities," in *Proceedings of 8th European Wave Tidal Energy Conference*, pp. 76–84, 2009.

[16] A. Clément, P. McCullen, A. Falcão, A. Fiorentino, F. Gardner, K. Hammarlund, G. Lemonis, T. Lewis, K. Nielsen, S. Petroncini, *et al.*, "Wave energy in europe: current status and perspectives," *Renewable and sustainable energy reviews*, vol. 6, no. 5, pp. 405–431, 2002.

[17] D. Valério, P. Beirão, and J. S. da Costa, "Optimisation of wave energy extraction with the archimedes wave swing," *Ocean Engineering*, vol. 34, no. 17-18, pp. 2330–2344, 2007.

[18] J. van Rij, Y.-H. Yu, and Y. Guo, "Structural loads analysis for wave energy converters," in *ASME 2017 36th International Conference on Ocean, Offshore and Arctic Engineering*, pp. V010T09A023–V010T09A023, American Society of Mechanical Engineers, 2017.

[19] F. d. O. Antonio, "Wave energy utilization: A review of the technologies," *Renewable and sustainable energy reviews*, vol. 14, no. 3, pp. 899–918, 2010.

[20] J. Falnes, "A review of wave-energy extraction," *Marine structures*, vol. 20, no. 4, pp. 185–201, 2007.

[21] D. Magagna, R. Monfardini, and A. Uihlein, "Jrc ocean energy status report 2016 edition," *Publications Office of the European Union: Luxembourg*, 2016.

[22] R. Yemm, D. Pizer, C. Retzler, and R. Henderson, "Pelamis: experience from concept to connection," *Philosophical Transactions of the Royal Society A: Mathematical, Physical and Engineering Sciences*, vol. 370, no. 1959, pp. 365–380, 2012.

[23] T. Whittaker and M. Folley, "Nearshore oscillating wave surge converters and the development of oyster," *Philosophical Transactions of the Royal Society A: Mathematical, Physical and Engineering Sciences*, vol. 370, no. 1959, pp. 345–364, 2012.

[24] S. Bozzi, G. Besio, and G. Passoni, "Wave power technologies for the mediterranean offshore: Scaling and performance analysis," *Coastal Engineering*, vol. 136, pp. 130–146, 2018.

[25] P. Le Tallec and J. Mouro, "Fluid structure interaction with large structural displacements," *Computer methods in applied mechanics and engineering*, vol. 190, no. 24-25, pp. 3039–3067, 2001.

[26] Z. Zang, Q. Zhang, Y. Qi, and X. Fu, "Hydrodynamic responses and efficiency analyses of a heaving-buoy wave energy converter with pto damping in regular and irregular waves," *Renewable Energy*, vol. 116, pp. 527–542, 2018.

[27] Y. Wen, W. Wang, H. Liu, L. Mao, H. Mi, W. Wang, and G. Zhang, "A shape optimization method of a specified point absorber wave energy converter for the south china sea," *Energies*, vol. 11, no. 10, p. 2645, 2018.

[28] S.-J. Kim, W. Koo, and M.-J. Shin, "Numerical and experimental study on a hemispheric point-absorber-type wave energy converter with a hydraulic power take-off system," *Renewable Energy*, vol. 135, pp. 1260–1269, 2019.

[29] A. S. Zurkinden, F. Ferri, S. Beatty, J. P. Kofoed, and M. Kramer, "Non-linear numerical modeling and experimental testing of a point absorber wave energy converter," *Ocean Engineering*, vol. 78, pp. 11–21, 2014.

[30] S. F. Estefen, X. Castello, M. I. Lourenço, and R. M. Rossetto, "Design analysis applied to a hyperbaric wave energy converter," in *Proceedings 11th International Symposium on Practical Design of Ships and Other Floating Structures*, 2010.

[31] *StarCCM+ 11.06 User's Guide*.

[32] P. K. Banerjee and R. Butterfield, *Boundary element methods in engineering science*, vol. 17. McGraw-Hill London, 1981.

[33] C. W. Hirt and B. D. Nichols, "Volume of fluid (vof) method for the dynamics of free boundaries," *Journal of computational physics*, vol. 39, no. 1, pp. 201–225, 1981.

[34] W.-X. Ren and H.-B. Chen, "Finite element model updating in structural dynamics by using the response surface method," *Engineering structures*, vol. 32, no. 8, pp. 2455–2465, 2010.

[35] S.-H. Kim and Y.-s. Park, "An improved finite difference type numerical method for structural dynamic analysis," *Shock and Vibration*, vol. 1, no. 6, pp. 569–583, 1994.

[36] J. Besseling, "The complete analogy between the matrix equations and the continuous field equations of structural analysis," in *International symposium on analogue and digital techniques applied to aeronautics: Proceedings*, pp. 223–242, 1964.

[37] M. Géradin and A. Cardona, *Flexible multibody dynamics: a finite element approach*. John Wiley Chichester, England; New York, USA, 2001.

[38] K. Van der Werff, "Kinematic and dynamic analysis of mechanisms, a finite element approach," 1977.

[39] T. Belytschko and B. Hsieh, "Non-linear transient finite element analysis with convected co-ordinates," *International Journal for Numerical Methods in Engineering*, vol. 7, no. 3, pp. 255–271, 1973.

[40] A. A. Shabana, "Flexible multibody dynamics: review of past and recent developments," *Multibody system dynamics*, vol. 1, no. 2, pp. 189–222, 1997.

[41] M. Milsted, "Cl dym and ih shames, solid mechanics: A variational approach, mcgraw-hill book company, inc, new york (1973) xix+ 556 pp.," *Journal of Sound Vibration*, vol. 34, pp. 576–578, 1974.

[42] T. Belytschko, W. K. Liu, B. Moran, and K. Elkhodary, *Nonlinear finite elements for continua and structures*. John wiley & sons, 2013.

[43] G. T. Mase, R. E. Smelser, and G. E. Mase, *Continuum mechanics for engineers*. CRC press, 2009.

[44] L. Wang, A. Kolios, L. Cui, and Q. Sheng, "Flexible multibody dynamics modelling of point-absorber wave energy converters," *Renewable energy*, vol. 127, pp. 790–801, 2018.

[45] D. Negrut, R. Rampalli, G. Ottarsson, and A. Sajdak, "On an implementation of the hilber-hughes-taylor method in the context of index 3 differential-algebraic equations of multibody dynamics (detc2005-85096)," *Journal of computational and nonlinear dynamics*, vol. 2, no. 1, pp. 73–85, 2007.

[46] H. M. Hilber, T. J. Hughes, and R. L. Taylor, "Improved numerical dissipation for time integration algorithms in structural dynamics," *Earthquake Engineering & Structural Dynamics*, vol. 5, no. 3, pp. 283–292, 1977.

[47] G. DNV, "Fatigue design of offshore steel structures," *Recommended Practice DNVGL-RP-C203*, vol. 20, 2016.

[48] D. Ion, K. Lorand, D. Mircea, and M. Karoly, "The equivalent stress concept in multiaxial fatigue," *Journal of Engineering Studies and Research*, vol. 17, no. 2, p. 53, 2011.

[49] B. J. Reinhart and S. Pfaff, "Wave analysis for rip current forecasting in southeast north carolina," *Technical Attachments, National Oceanic and Atmospheric Administration*, 2016.